

THE TOLMAN SURFACE BRIGHTNESS TEST FOR THE REALITY OF THE EXPANSION. V. PROVENANCE OF THE TEST AND A NEW REPRESENTATION OF THE DATA FOR THREE REMOTE *HST* GALAXY CLUSTERS

Allan Sandage

*The Observatories of the Carnegie Institution of Washington,
813 Santa Barbara Street, Pasadena CA, 91101*

Details sire the complications: old Chinese saying

ABSTRACT

A new reduction is made of the *HST* photometric data for E galaxies in three remote clusters at redshifts near $z = 0.85$ in search for the Tolman surface brightness (SB) signal for the reality of the expansion. Because of the strong variation of SB of such galaxies with intrinsic size, and because the Tolman test is about surface brightness, we must account for the variation. In an earlier version of the test, Lubin & Sandage calibrated the variation out. In contrast, the test is made here using fixed radius bins for both the local and remote samples. Homologous positions in the galaxy image at which to compare the surface brightness values are defined by radii at five Petrosian η values ranging from 1.0 to 2.0. Sérsic luminosity profiles are used to generate two diagnostic diagrams that define the mean SB distribution across the galaxy image. A Sérsic exponent, defined by the r^n family of Sérsic profiles, of $n = 0.46$ fits both the local and remote samples. Diagrams of the dimming of the $\langle SB \rangle$ with redshift over the range of Petrosian η radii shows a highly significance Tolman signal but degraded by luminosity evolution in the look-back time. The expansion is real and a luminosity evolution exists at the mean redshift of the *HST* clusters of 0.8 mag in R_{cape} and 0.4 mag in the I_{cape} photometric rest-frame bands, consistent with the evolution models of Bruzual and Charlot.

Subject headings: cosmology: observations — galaxies: clusters: general

1. INTRODUCTION

In one of the outstanding ironies in the history of observational cosmology, Hubble, even in his last years, expressed doubts about the reality of the expansion. His reasons were

based on what he considered to be anomalies in the correlation of apparent magnitudes and redshifts (the Hubble diagram) and in his galaxy counts (Hubble 1934, 1936), when both are corrected for the effects of redshifts on the apparent magnitudes. These corrections, the K terms, are calculated by shifting an assumed spectral energy curve of the mean mixture of galaxy types through the fixed photometric band pass of the detector. Applying his calculated corrections to his redshift diagram and his $N(m)$ count data gave Hubble what seemed to be unacceptable results if the expansion is real.

His most direct statements were these.

(1). “It is evident that the observed result, [of applying a blue K correction of 2.94 z mag] is accounted for if the redshifts are not velocity shifts”. . . . [the data are consistent but only if] “the expansion and spatial curvature are either negligible or zero” (Hubble 1936, p. 542).

(2). In considering the redshift-distance relation, “The inclusion of recession factors [to the magnitudes] would displace all the points [in the Hubble diagram] to the left [higher redshifts at a given magnitude], thus destroying the linearity of the law of redshifts” (Hubble 1937).

(3). . . . “if redshifts are not primarily due to velocity shifts . . . [then] the velocity-distance relation is linear, the distribution of nebulae is uniform, there is no evidence of expansion, no trace of curvature, no restriction of the time scale.” [But] “the unexpected and truly remarkable features are introduced by the additional assumption that redshifts [actually do] measure recession. The velocity-distance relation deviates from linearity by the exact amount of the postulated recession. The distribution departs from uniformity by the exact amount of the recession. The departures are compensated by curvature which is the exact equivalent of the recession. Unless the coincidences are evidence of an underlying necessary relation between the various factors, they detract materially from the plausibility of the interpretation. . . . the small scale of the expanding model both in space and time is a novelty, and as such will require rather decisive evidence for its acceptance” (Hubble 1936, p. 553/4).

(4). And finally in his Darwin Lecture in 1953, only a few months before his death: “When no recession factors are included, the law will represent approximately a linear relation between redshift and distance. When recession factors are included, the distance relation [becomes] non-linear.” [If no recession factor is included] “the age of the universe is likely to be between 3000 and 4000 million years, and thus [again with no recession factor] comparable with the age of the rock crust of the Earth” (Hubble 1953). (Here concerning the time scale, Hubble clearly was factoring in the beginning of the major correction to his distance scale that would eventually reach a ratio between 7 and 10 for the new scale to the

old. Clearly, in 1953 he was beginning to accept that his value of the Hubble constant must be considerably revised downward, based, as it was in 1953, on Baade’s revision of Hubble’s distance to M31 by a scale factor close to 2).

It is now known that these arguments against a true recession are incorrect. Details of why have been variously set out elsewhere, the most recent in several reviews (Sandage 1995, 1998). The essence of the case is threefold.

(A). The K corrections for the effects of redshifts on apparent magnitudes used by Hubble are incorrect because he assumed a black body spectral energy distribution (SED) of 6000 K temperature whereas Greenstein (1938) had shown already in 1938 that the correct ‘color temperature’ of the bulge of M31 is closer to 4200 K. A directly observed template SED for E galaxies was not measured until beginning in 1968 (Oke & Sandage 1968; Whitford 1971; Schild & Oke 1971; Code & Welch 1979), and eventually for galaxies of other morphological types. Examples include the works by Wells (1973), Pence (1976), Coleman, Wu, & Weedman (1980), and Yoshii & Takahara (1988), and thereafter by many others in various pass bands, summarized elsewhere (Sandage 1988, § 4.2).

(B). Hubble’s magnitude scales were extrapolations of the Mount Wilson Catalogue of Photographic Magnitudes (Seares, Kapteyn, & van Rhijn 1930), which themselves needed systematic corrections fainter than about 16 apparent blue magnitude (Stebbins, Whitford, & Johnson 1950; Sandage 2001). Baade had often called Hubble’s approximations “enthusiastic magnitudes”, not out of derision but as a tribute to Hubble’s skill in devising by practical methods what he needed in his reconnaissance studies of difficult problems.

(C). Hubble’s definition of redshift distance as $D = cz/H_0$ is the intuitive choice but is incorrect in the standard model of cosmological parameters. The exact formulation was not made until the fundamental paper by Mattig (1958). The difference between Hubble’s assumption and the exact formulation of metric coordinate distance for different geometries and redshifts is large, as seen in Figure 4 of Sandage (1998).

The consequence of these developments has been that Hubble’s reticence to accept the redshift-distance relation as due to real recession is no longer valid. There is almost universal acceptance that the redshift phenomenon which increases linearly with distance is due to a real recession. Of the several reasons, the most direct is the excellent agreement in the three time scales of (a) the expansion age once the Hubble constant is known, (b) the age of the oldest globular clusters in the Galaxy, and (c) the age of the chemical elements. All three average about 14×10^9 years.

Other less direct tests, less direct because they require more complicated assumptions concerning a hot early universe giving rise to the 3° MWB, include the observation that the

temperature of the MWB is hotter at high redshift as we look back in time (Songaila et al. 1994; Srianand, Petitjean, & Ledoux 2000; Molaro et al. 2002), the acoustic waves in the correlation of the fluctuation in the MWB, and, of course the MWB itself. Although in a minority, there are still astronomers who offer alternate explanations of these latter tests in their questioning of the standard model of a hot early universe; yet the time scale agreement remains the decisive test (Sandage 1968) on which there is now such a large literature as to deny an adequate summary here.

Nevertheless, a true expansion where the redshifts are cosmological, not due to “some unknown law of nature” as favored by Hubble, is itself such a remarkable proposition that decisive proofs are still of interest, even if only as academic curiosities now.

The Tolman surface brightness test is particularly interesting because its principle is so clear as to give a major predicted difference in observational data between an expanding manifold and a stationary one where the redshift would then be due to “an unknown law of nature”. Tolman (1930, 1934) discovered the effect that the surface brightness of a “standard” radiating object that is receding with redshift z will be fainter than a similar stationary “standard” object at rest by $(1+z)^4$. However, if the manifold is stationary but nevertheless has a redshift due to an “unknown law of nature”, the factor is only $(1+z)$. The test, as set out in theory by Tolman, is described again in Hubble & Tolman (1935) and is derived heuristically elsewhere (eg. Sandage 1961, 1974, 1995).

The test, simple in principle is difficult in practice because there are no simple “standard” galaxies to compare with each other, one at high redshift and the other at small. The difficulty of using E galaxies for the test has been discussed elsewhere (Sandage & Perelmuter 1990a,b, 1991; Sandage & Lubin 2001; Sandage & Lubin 2001a,b,c, hereafter LS01a,b,or c) and is not repeated here.

The first attempt at the test was made by Sandage & Perelmuter using ground based data in the references just cited (hereafter SP90a,b; SP91). The purpose of the present paper is to continue the discussion made in a second attempt of the test by Sandage & Lubin using *HST* data (LS01c) by showing more directly that a strong Tolman signal exists in three remote clusters observed with *HST* by Oke, Postman, & Lubin. Their photometric data are published in papers by various permutations of the order of the authors (OPL 1998; PLO 1998, 2001; Lubin et al. 1998, 2001). The analysis by LS01c remains valid that the Tolman signal exists, but the reductions and the representation of the data are different here.

2. THE PROVENANCE OF THE TOLMAN TEST USING *HST*

Extensive planning related to constructing and deploying a large space telescope had its beginnings in the early 1960s, although the concept had already been set out 20 years earlier (Spitzer 1946) in the United States and two decades earlier by Oberth (1923) in Germany. The project, accepted by NASA in the late 1950s, was first called the *LST* for Large Space Telescope, but more appropriately known to the underground as the Lyman Spitzer Telescope because Spitzer had done so much to promote the idea.

Many planning sessions occurred to define the scientific goals, and the means to achieve them. By the mid 1960s a NASA department for the *LST* project was formed with Nancy Roman as its head. The chief scientist had also been appointed, the first of which was Charles O’Dell. In these early days of planning and of selling the project to the astronomical community and especially to Congress for funding, the importance of Roman and O’Dell cannot be overstated.

When it became apparent that an *LST* could be built and operated remotely, based on the experience and successes of the Orbiting Astronomical Observatories project led by the Grumman Aerospace Corporation with their chief engineer F. P. Simmons as coordinator, serious scientific and technical workshops were convened to advance the project. One such conference was held in 1974 at the Park-Sheraton Hotel in Washington DC, organized by Simmons, then at the McDonald-Douglas Astronautics Company. In a three day meeting, astronomers and engineers made presentations to Roman, O’Dell, and the astronomical and technical community on a variety of scientific projects ripe for the *LST*. Space engineers from 12 aerospace companies also discussed the means to achieve the goals. The astronomers giving papers were Spitzer, J. L. Greenstein, I. King, E. M. Burbidge, L. W. Fredrick, G. Neugebauer, G. Herbig, J. Bahcall, Harlan Smith, and the writer.

Together with other projects for *LST* in observational cosmology, I discussed the requirements of spatial resolution and input flux needed to make the Tolman surface brightness test. Details were set out for a particular form of the test, comparing the ratio of a suitably defined isophotal diameter (the angular diameter to a particular isophotal level) in an E galaxy to a suitably defined metric diameter (the angular diameter to a given number of parsecs) for the same galaxy. I concluded that the *LST* would be an ideal instrument to make the test with its proposed 3-meter aperture and a spatial resolution of 0.05 to 0.1 arc sec. Of course, not known at the time was the way that surface brightness over the image of E galaxies at some standard diameter varies systematically with intrinsic size and absolute magnitude, or indeed how to define a series of “standard diameters” within which to measure the surface brightness. These complications were to be encountered later. Nevertheless, the project with *LST* was set out as a serious observing plan that was ideal for the capabilities of the

proposed telescope. It has worked out that way, where the Tolman test with *HST* has been done (LS01a,b,c), 25 years beyond the initial proposal for a space experiment.

The photometric data for three remote clusters observed by Oke, Lubin, and Postman, cited earlier as OPL 1998; PLO 1998, 2001; Lubin et al. 1998, 2001, and reduced in the way described in LS01a,b,c are again used here. What is different in the analysis is threefold.

(1). A more comprehensive calibration of the local data on E galaxy surface brightness as function of intrinsic radius is made in § 3, reaching to smaller radii than was done in LS01c. This is necessary because the galaxies in the *HST* clusters are at the faint end of the luminosity function of the first few ranked galaxies in the calibrating sample taken from Postman & Lauer (1995, hereafter PL95) and from Table 1 of SP91 used in a first study of the test. This new calibration of the $\langle SB \rangle$ -radius correlation avoids a less certain extrapolation to the necessary smaller radii for the three remote clusters than we made in SL01 (Table 3 there).

(2). The variation of surface brightness across the E galaxy image for particular Petrosian (1976) sizes, for both the local calibrating galaxies and the remote sample, is explicitly shown as a function of intrinsic Petrosian radii. The data are divided into groups of different mean intrinsic radii so as to isolate the large systematic variation of the mean surface brightness with radius (or absolute magnitude for M brighter than $M_V = -20$, eg. see Figs. 1 and 2 of SP91). This dependence of the $\langle SB \rangle$ zero point on intrinsic radius at a given standard size degrades a raw Tolman signal and must be calibrated out. Much of § 3 is devoted to determining these properties of the Sérsic profiles.

(3). We show in § 3.4 that the Sérsic profile with an exponent of 0.46, rather than a de Vaucouleurs value of 0.25, fits our local sample over its range of intrinsic radii. The systematic deviation of the profile exponent from a de Vaucouleurs $r^{0.25}$ value with intrinsic radius is strong and is mapped. The variation of n with radius is the same as discovered by Binggeli & Jerjen (1998, Fig. 2).

3. PROPERTIES OF SÉRSIC LUMINOSITY PROFILE FUNCTIONS IMPORTANT FOR THE TOLMAN TEST

3.1. The Petrosian Radius Function

In the original 1974 proposal, the test was to be made by comparing the ratio of isophotal to metric diameters for E galaxies at zero redshift to those with redshift z . For the high redshift galaxies, the ratio of $r(\text{isophotal})$ to $r(\text{metric})$ at a given metric diameter should

decrease with increasing redshift if a Tolman signal exists. However, the test is difficult to apply because the metric diameters depend on the world model. We would also have to apply the K correction for the effect of redshift on the isophotal surface brightness values. We wish to avoid these problems at this stage in the data reductions. A formulation of the test using Petrosian radii which avoids these problems is used here instead.

Some of the remarkable properties of the Petrosian radius function have been discussed elsewhere (SP90a; Kron 1995; Sandage 1995; SL01) and are only summarized here.

Two equivalent definitions are these. (1) A Petrosian radius is a distance from the center of an image where the surface brightness (SB), averaged over the image that is interior to that radius is greater than the profile SB at that radius by a fixed number of magnitudes. (2) It can be shown (Djorgovski & Spinrad 1981; SP90a) that this is the same number that is calculated from the slope of the growth curve, as,

$$\eta \text{ (in mag)} = 2.5 \log(5d \log r / d \text{ mag}), \quad (1)$$

where the growth curve is the summed intensity (in magnitudes) out to that r and its slope at r is $d \text{ mag} / d \log r$. Expressed as the slope in intensity units, as in PL95, $\alpha (= d \log L / d \log r)$, which is used by some authors. Of course, $\eta(\text{in mag}) = 2.5 \log 2 / \alpha$.

The Petrosian η function for radii was used throughout the first and second attempts to make the Tolman test (SP90a,b, SP91; SL01 and LS01a,b,c).

3.2. The Variation of Petrosian η Radii Along the Hubble Sequence From E to Sm Types

It is of interest to display the η function at various ratios of radii to the effective (the half-light) radius, r_e . Because the luminosity profiles of galaxies are so different along the Hubble sequence, there is a systematic variation of η with morphological type, as calculated using equation (1) using the growth curves from Table 11 of the Third Reference Catalogue (de Vaucouleurs et al. 1991, the RC3). The results are listed in Table 1 as function of $\log r/r_e$, and shown in Figure 1. The T coding for the morphological types is the same as in the RC3. The even numbered columns of Table 1 are the growth curve magnitudes. The odd numbered columns are the η radii at the listed $\log r/r_e$ values.

In the next subsection we show that the entries in Table 1 for the E ($T = -5$) galaxies is close to, but not identical with the de Vaucouleurs $r^{0.25}$ profile. We also show there that the η values for the Sm ($T = 9$) galaxy type is nearly identical with the exponential intensity profile whose Sérsic exponential index is $n = 1$.

3.3. The η , $\log r/r_e$ and $\log r/r(\eta = 2)$ Relations for the Family of Sérsic Luminosity Profiles for E Galaxies

It is now well known (citations later in this section) that the de Vaucouleurs $r^{0.25}$ luminosity profile only fits E galaxies near the bright end of the E galaxy luminosity function that themselves are not cD subtypes (Oemler 1974, 1976). Sérsic (1968) generalized the de Vaucouleurs $r^{0.25}$ profile with the function,

$$\log[B(r/r_e)/B(r_e)] = -b_n[(r/a)^n - 1], \quad (2)$$

where a is a fixed radius to make the radius factor scale free, n is the Sérsic exponent, and b_n is calculated to make the half-light radius occur at the value of $a = r_e$. The de Vaucouleurs profile is a special case with $n = 0.25$ and $b_n = 3.33$.

The adopted b_n values, listed in Table 2, were calculated by numerical integration of equation (2) to generate growth curves in r/a , such that $a = r_e$ for each of Sérsic profiles with n values of 0.15, 0.2, 0.25, 0.4, 0.46, 0.6, 1.0, and 1.5. The growth-curve magnitudes and Petrosian η values in Table 3 are at the listed r/r_e values for these n values. The listings for $T = -5$, and $n = 0.25$ and 0.46 are the same as in Table 1.

Figure 2 shows the variation of η with r/r_e for the various n values from Table 3. If all E galaxies had a fixed luminosity profile, such as that for the de Vaucouleurs $r^{0.25}$ special case, Table 3 would be germane only to the E galaxy types for the $T = -5$ column. However, in papers cited below, it has become known that the Sérsic n exponent varies systematically with absolute magnitude in E and dE galaxies, ranging from 0.15 to 1.5 as the absolute magnitude varies between $M_B = -23$ and -13 .

The progression of $\langle SB \rangle$ with absolute magnitude was discovered by many authors (eg. Oemler 1973, 1974; Kormendy 1977, 1987; Strom & Strom 1978a,b,c; Michard 1979; Thomsen & Frandsen 1983; Binggeli, Sandage, & Tarenghi 1984; Choloniewski 1985; Schombert 1986; Ichikawa, Wakamatsu, & Okamura 1986; Caldwell & Bothun 1987; Djorgovski & Davis 1987; Ferguson & Sandage 1988; Impey, Bothun, & Malin 1988; Caon, Capaccioli, & D’Onofrio 1993) and we suspect many others. If the deviation from the classical Hubble or de Vaucouleurs E galaxy profiles can be described by Sérsic functions, which we prove in the next section, it is this deviation that is listed in Table 3.¹

¹This paper was finished in first draft in February, 2009 and was at the stage of first revision when Francois Schweizer drew my attention to the comprehensive account by Kormendy et al. (2009) of using Sérsic profiles for E galaxies. These authors develop, as we do here, various useful properties of the Sérsic r^n functions and conclude, as we also, that Sérsic profiles with their range of n values fit the observed E

But before giving the proof, we first rearrange Table 3 to use η rather than r/r_e as the independent variable. The table is also renormalized to change the fiducial radius from the half-light radius to the radius at $\eta = 2$, hereafter called $r(2)$. The change is made because it will be more convenient in § 5 to use $r/r(2)$ to compare surface brightness levels at various points rather than r_e . To this end, Table 4 is reconstituted by a graphical interpolation of Table 3, and then defines the radius at $\eta = 2$ to be the zero point of the coordinate radius. Figure 3 shows the data from Table 4 for the ratio of the various $r(\eta)$ radii to $r(2)$. This diagnostic diagram will be often used later to compare observational data for local and the *HST* cluster galaxies.

3.4. Oemler Profiles

But before comparing the entries in Tables 3 and 4 with observed E galaxy profiles, it is of interest to compare the Sérsic profiles with those of Oemler (1974, 1976). Oemler’s function embrace a family based on a modified Hubble profile with various strengths of a luminosity turndown at large radii. The Oemler profiles have the equation,

$$B(r)/B_0 = \frac{\exp(-r/\alpha)^2}{(1 + r/\beta)^2} \quad (3)$$

where α and β are fitting parameters. This function is illustrated in SP90a where the resulting family, relative to the Hubble profile, is shown in Figures 2 and 3 of that paper. The profiles are generated by varying the α/β ratio, and is made scale free by using r/β as the radius measure.

Note that the denominator on the right of equation (3) is the Hubble law. The numerator is the added decay factor making the integrated growth curve finite, which the raw Hubble law does not. The similarity and the differences with the Sérsic family that is used here is in Figure 4, taken from Table 5 where the η , $r/r(\eta = 2)$ Oemler profiles are listed for α/β ratios of 10, 30, 60, and 100. The $T = -5$ relation is copied from Table 1 but is modified in an obvious way to be a function of $r/r(2)$ rather than r/r_e . Three Oemler profiles from Table 5 are shown and are compared with the $T = -5$ profile from Table 1 and with the

galaxy surface photometry remarkably well. However, the treatment differs in the two works. We develop the properties of the Sérsic functions in terms of Petrosian η radii to define homologous regions of the image for galaxies of different absolute magnitude. Kormendy et al. do not use Petrosian radii because they have no need in their study of origins to define similar points over an E galaxy image, which we must for the Tolman test. Such points are naturally given by Petrosian radii. The sometimes parallel conclusions, here and by Kormendy et al., of the properties of Sérsic functions, agree.

$n = 0.46$ Sérsic profile from Table 3. The fit of the $T = -5$ data with the Oemler profile for $\alpha/\beta = 30$ for η between 1 and 2 is excellent, after which the fit must be made to an α/β ratio of 100 for η between 2 and 3.5. The fit of the $n = 0.46$ Sérsic profile is excellent for an Oemler profile of $\alpha/\beta = 10$ for $\eta < 2$, after which an α/β ratio of 30 must be used. Table 5 has been calculated in an obvious way from equation (1) using Table 1 of SP90a for the slope of the Oemler growth curves.

Our reason for discussing the Oemler profiles here is that they are a natural generalization of the Hubble single parameter profile that was standard for many years, and it was the Hubble profile with its scale factor, a , that was discussed in proposing the Tolman test at the *LST* meeting in 1974.

Return now to the Sérsic profiles to display the surface brightness- η properties of the Sérsic function.

3.5. Surface Brightness vs. η for Sérsic Profiles Normalized to $\eta = 2$

Because the Tolman test concerns surface brightness, it is necessary to cast the Sérsic profiles in Tables 3 & 4 and Figure 3 in terms of surface brightness. The relative shape of the SB profiles in the Sérsic family is the subject of this section.

Once the growth curve of a particular intensity profile is known, the surface brightness averaged over a given radius follows from,

$$\langle SB(\eta) \rangle = 2.5 \log(\pi r_\eta)^2 + m(\eta)_{GC}, \quad (4)$$

where the first term on the right is the area expressed in mag per square arc sec, and the other is the magnitude from the growth curve (GC) at the particular value of η . In practice, if we want only the run of $\langle SB \rangle$ with η , normalized to say $\eta = 2$, it is sufficient to use

$$\Delta \langle SB \rangle_{\eta=2} = 5 \log r/r(2) + m(\eta)_{GC}. \quad (5)$$

Mean $\langle SB \rangle$ relative to that at $\eta = 2$ for the Sérsic family using equation (5) are listed in Table 6 and shown in Figure 5 for η values from 1.0 to 4.0. The $\langle SB \rangle$ values for E galaxies, calculated from the observed $T = -5$ growth curve, are also listed in column (5). Figure 5 is the second diagnostic diagram that will be used in later sections.

The close agreement of the listed $\langle SB \rangle$ for $T = -5$ with the $n = 0.25$ de Vaucouleurs profile is one of the proofs we are seeking that Sérsic profiles have relevance for E galaxies. A generalization of the proof for different absolute magnitudes for E galaxies is in the next section.

4. THE VARIATION OF THE SURFACE BRIGHTNESS WITH INTRINSIC RADIUS AT VARIOUS η VALUES FOR LOCAL GALAXIES IN THE VIRGO, FORNAX, AND COMA CLUSTERS

The relevance of the Sérsic family of profiles for observations of real E galaxies was shown in the last section, but only for the case of galaxies with the $T = -5$ growth curve. The E galaxies used to define the $T = -5$ growth curve (Table 11 of the RC3) are those of the average absolute magnitude for such galaxies that exist in the catalogs of aperture photometry that were available when the RC3 was compiled. However, because the luminosity profile of E galaxies, and hence the Sérsic n value, is such a strong function of linear size, we must generalize the RC3 $T = -5$ growth curve over a large range of absolute magnitude and intrinsic size.

Data on the observed profiles for local galaxies that span a range of five magnitudes are in the literature for the Virgo, Fornax, and Coma clusters. The photometry is by Fraser (1977), King (1978), Hodge (1978), Ichikawa, Wakamatsu, & Okamura (1986), Schombert (1986), Jedrzejewski (1987), and Vigroux et al. (1988) for Virgo, by Schombert (1986) and Caldwell (1987) for Fornax, and by Oemler (1976) for Coma. η was calculated in SP90b from these data using equation (2). A diagram similar to Figure 5 in SP90a was drawn for each galaxy showing the published profile, the growth curve, and η calculated at the listed radii. The $\log r$ (arc sec) for η values of 1.0, 1.3, 1.5, 1.7, 2.0, 2.5, 3.0, 3.5, and 4.0 were determined graphically from these diagrams. The surface brightness averaged over the area interior to the listed radii is listed in Tables 1-3 in SP90b at each η value.

Data for 153 cluster galaxies were determined in this way; 83 in Virgo, 20 in Fornax, and 42 in Coma. The data cover a range in absolute magnitude from $M_B(T) = -23$ to -13 and a range of intrinsic radii from $\log R(\eta = 2)$ of 3.3 to 5.1 (pc), and are listed in Tables 1–3 in SP90b. Where needed, we adopted distance moduli of 31.7 for Virgo, 31.9 for Fornax, and 35.5 for Coma.

Calculations were made from these data for the $\log r(\eta)/r(2)$ radius ratios and the $SB(\eta) - SB(\eta = 2)$ surface brightness differences relative to the values at $\eta = 2$ over the range of η values from 1.0 to 4.0. These data permit the observations to be compared with the expectations in the diagnostics Figures 3 & 5 using the family of Sérsic profiles.

Based on the strong correlation of the Sérsic n exponent with absolute magnitude discovered by Binggeli & Jerjen (1998, their Fig. 2), there must be a correlation of $\log r(\eta)/r(2)$ with intrinsic radius if the Sérsic theoretical profiles are good fits to the observed profiles. This expectation for the Virgo, Fornax, and Coma cluster galaxies is verified in Figures 6 & 7 where both $\log r(1)/r(2)$ and $\langle SB(2) \rangle - \langle SB(1) \rangle$ are plotted against $\log R(\eta = 2)$. Be-

cause these ratios change systematically with $\log R(2)$, and because they are both functions of Sérsic n at any given η (Figs. 3 & 5 here), n must itself be a function of $\log R(2)$, and therefore of absolute magnitude. Figure 2 of Binggeli & Jerjen (1998) is explicit, showing that the Sérsic n varies between 0.15 to 1.5 as the apparent B_T magnitude in Virgo cluster E galaxies change between 9 and 18, or $M_{B(T)}$ between -22.7 and -13.7 .

Interpolating in Table 4 by using Figure 6 for $\log r(1)/r(2) = -0.5$, we determine that the Sérsic exponent is 0.46 ± 0.02 at $\log R(2) = 3.9$, which is the average for the *HST* clusters. This interpolation shows that n increases as $R(2)$ decreases, reaching the exponential value of $n = 1$ near apparent magnitude $B(T) = 16$ ($M_T = -15.7$) in the Virgo cluster (see also Binggeli & Jerjen 1998), well into the dE morphological types.

We have also tested the adequacy of the Sérsic profiles using the much larger sample of 178 galaxies in 78 local Abell clusters studied by SP91. The data are in the V band for this independent sample. They were analyzed in the way just described for the Virgo/Fornax/Coma clusters. The observed profiles are from Oemler (1976), Thuan & Romanishin (1981), Malumuth & Kirshner (1985), and Schombert (1987). Here, the intrinsic radius at $\eta = 2$ varies from $\log R(2) = 4.0$ to 5.5. From § 6 later, we see that this range is larger than the average $\langle \log R(2) \rangle = 3.9$ for the three remote *HST* clusters, and the difference must be accounted for, as is done in § 5 and 6.

A third independent sample of local cluster galaxies is from PL95 who again used first ranked E galaxies in local Abell clusters. There are 128 galaxies in the PL sample whose intrinsic radii are again large, ranging from $\log R(2)$ of 4.0 to 5.5.

Using these data from the three independent sources, we drew diagrams (not shown) similar to Figures 6 & 7 over the additional range of η values from 1.3, 1.5, to 1.7. Comparing the variation of $\log r(\eta)/r(2)$ and $SB(\eta) - SB(2)$ with Figures 3 & 5 for the Sérsic family as the n exponent is varied shows that the Sérsic models are excellent fits to actual E galaxy profiles over the entire range of η and Sérsic n values, consistent with Figure 2 of Binggeli & Jerjen (1998) and with the conclusion of Kormendy et al. (2009).

This completes the proofs that the Sérsic family of profiles fit the observed E galaxy data over the total range of E galaxy absolute magnitudes, and that the curves in Figures 3 & 5 for the Sérsic family can be used to model the profiles of real galaxies. The systematically varying n values can be determined by fitting the data to these two diagnostic diagrams, as we do in Figure 15 later.

5. CALIBRATION OF THE RELATION BETWEEN SURFACE BRIGHTNESS AND INTRINSIC RADIUS USING LOCAL E GALAXIES

That the surface brightness of E galaxies varies strongly and systematically with intrinsic radius, becoming brighter as the radius decreases, has variously been rediscovered in the many papers cited earlier, perhaps earliest seen in photographs by Burbidge, Burbidge, & Crampin (1964, BBC). The sense of fainter $\langle SB \rangle$ for larger $R(2)$ values of E galaxies, seen so well in the BBC photographs, holds until $\log R(2) = 3.8$, where the relation reverses (Binggeli et al. 1984; SP90b, Fig. 14) for the faint dE galaxies.

We showed in SL01 that the variation of SB with intrinsic radius for E galaxies is also well defined at the η values of 1.0, 1.3, 1.5, 1.7, and 2.0. The spread at a given radius is one magnitude whereas the total range of SB between $\log R(2)$ of 4.2 and 5.4 is 4 magnitudes (Fig. 2 of SL01). Because the Tolman test is about surface brightness, we must either calibrate out this variation, or we must make the test by comparing the SB of the data set at the same $R(\eta)$ radii. We chose the latter here.

The analysis in SL01 provides the first step in determining the zero point of the SB-intrinsic radius relation for local galaxies. The data listed in Table 1 of that reference are η , $\langle SB \rangle$, and intrinsic size for 118 first ranked local Abell clusters. These have been calculated from equations (1), (4), and (5) using the observed growth curves of PL95 with $H_0 = 50$.

The R magnitudes by Postman & Lauer are on the Cape/Cousins near red photometric system as realized by Landolt (1983, 1992). The R_{cape} band pass differs from R_J of Johnson (1965), which is identical to the $r(S20)$ system of Sandage & Smith (1963) that I used for all the Mount Wilson/Palomar near-red photometry of first ranked cluster galaxies with S20 photocathodes in the 1970s (eg. Sandage 1972, 1973). That photometric R system has now been largely replaced in the literature by the Cape/Cousins $(RI)_{\text{cape}}$ system because of the work of Landolt with his all-sky $UBV(RI)_{\text{cape}}$ standards. The difference in zero point between the R_{cape} and R_J systems is 0.26 mag at the color of local E galaxies, with R_{cape} being fainter at this color (Sandage 1997). The $\langle SB \rangle_{R_{\text{cape}}}$ and $\log R(\eta)$ data for the PL sample are in Table 1 of SL01.

Least squares linear fits to the $\langle SB \rangle$, $\log R$ data of Postman & Lauer are in Table 2 of SL01 and shown in Figure 2 there for η values of 1.3, 1.5, 1.7, and 2.0. These linear fits are valid only for $\log R > 4.0$. The $\langle SB \rangle$ data have been reduced to zero redshift by making them brighter by 0.16 mag than the values measured by PL95, determined by the method described in SL01.

The linear correlation of $\langle \text{SB} \rangle$ and size for $\eta = 2.0$ for zero redshift, is,

$$\langle \text{SB}(2) \rangle_{R_{\text{cape}}} = 2.97 \log R(2)_{50} + 8.53, \quad (6)$$

valid for $\log R(2)$ (pc) $> 4.3(H_0 = 50)$. The redshifts are small enough that the value of the spatial curvature, q_0 , is inconsequential.

The extension of equation (6) to $\log R(2) < 4.3$ is nonlinear, bending toward fainter $\langle \text{SB} \rangle$ at the smaller radii, shown in Figures 1 & 2 of SL01. It was accounted for there by a nonlinear addition to equation (6) for $\log R(2) < 4.4$. A first approximation for the correction was made from Table 3 in SL01. It is revised in Table 7 here. The correction is smaller than in SL01 by 0.3 mag at $\log R(2) = 3.4$, the difference decreasing to zero at $\log R(2) = 4.4$. The new corrections here are derived from the combined $\langle \text{SB} \rangle$, $\log R$ correlations in the Virgo, Fornax, and Coma clusters, discussed above, by a better spline connection of the cluster data from SP90b above and below $R(2) = 4.4$ (pc).

A second calibration, independent of equation (6), is made using the extensive V band data from Table 1 of SP90b, discussed earlier. The least squares regression of SB_V on $\log R(2)_{50}$ for the 178 galaxies in this earlier sample is,

$$\text{SB}_V(2) = 2.89 \log R(2) + 9.53, \quad (7)$$

reduced to zero redshift and valid for $\log R > 4.3$. The nonlinearity for $\log R < 4.3$ ($H_0 = 50$) is clearly seen (not shown) in these data, needing again the Table 7 correction for the smaller radii.

To compare (7) with equation (6) we change the slope to 2.97 and adjust the zero point, giving,

$$\text{SB}_V(2) = 2.97 \log R(2) + 9.17. \quad (8)$$

again valid only for $\log R(2) > 4.3(H_0 = 50)$. With these changes, equation (8) is everywhere within 0.08 mag of equation (7) over the range of $\log R$ between 4.0 and 5.0.

To compare equation (8) in V with equation (6) in R we need the color index, $(V-R)_{\text{cape}}$, for E galaxies with linear sizes of $\log R(2)$ between 4.0 and 5.0. The $(V-R)$ color for such giant E galaxies have been determined from the catalog of growth curves in R and I by de Vaucouleurs & Longo (1988) for a variety of photometric systems. Choosing from those that are on the Cape/Cousins system (listed as R' and I' in their catalog) for a sample of 17 local $T = -5$ galaxies with 66 measurements gave the mean color indices of $(V-R)_{\text{cape}} = 0.57 \pm 0.003$, and $(R-I)_{\text{cape}} = 0.64 \pm 0.003$. These are nearly identical with the values by Poulain & Nieto (1994) from a larger sample.

Applying $V - R = 0.57$ to equation (8) gives,

$$\text{SB}(2)_{R_{\text{cape}}} = 2.97 \log R(2) + 8.60, \quad (9)$$

for local E galaxies with $\log R(2) > 4.3$ ($H_0 = 50$). This is within 0.08 mag of the $\langle \text{SB} \rangle$, $\log R(2)$ calibration in equation (6) which is based on the independent photometry of Postman & Lauer. In what follows we adopt equation (9), and correct it by Table 7 for smaller radii.

Table 8, based on equation (9), corrected by Table 7, is our final adopted calibration for local zero redshift E galaxies for the nonlinear relation between $\log R(2)$ and $\langle \text{SB} \rangle$. The entries are calculated from the $\langle \text{SB} \rangle_R$ values just described using $(V - R)_{\text{cape}} = 0.57$ and $(R - I)_{\text{cape}} = 0.64$.

6. SURFACE BRIGHTNESS PROFILES FOR THE THREE *HST* CLUSTER GALAXIES COMPARED WITH THE LOCAL SAMPLE: THE TOLMAN TEST

Surface brightness magnitudes averaged over $R(\eta)$, the $R(\eta)$ sizes, and absolute magnitudes are listed in Tables 2–4 of LS01c for 34 galaxies in the three *HST* clusters. The data in LS01b show that the accuracies of η and $\langle \text{SB} \rangle$ are better than 2% at radii between 0.1 and 1 arc sec. The intrinsic R sizes for the database range from $\log R(2) = 3.45$ to 4.20 ($H_0 = 50, q_0 = 1/2, \Lambda = 0$), with a mean of 3.9.

Because of the strong variation of $\langle \text{SB} \rangle$ with intrinsic size, which we have been emphasizing, we have divided the galaxies in the *HST* clusters into three bins of different intrinsic radii, and make the Tolman test in each bin separately to compensate for the variation.

Table 9 lists the $\langle \text{SB} \rangle$, $\log R(\eta)$ data at the η values of 1.0, 1.3, 1.5, 1.7, and 2.0 for the three radius bins in *HST* Cl 1324+3011. The root data are from Table 3 of LS01c. The bottom entries are the mean values.

To make the Tolman test we need the $\langle \text{SB} \rangle$, $\log R(\eta)$ relation for galaxies of zero redshift at the mean $\log R(2)$ for the three *HST* radius bins in Table 9. An example, reading from Table 9, is that the mean radius at $\eta = 2$ for the largest radius group in Cl 1324+3011 is $\log R(2) = 4.087$ (in parsecs).

The $\langle \text{SB} \rangle_I$ -radius relation at $\eta = 2.0$ and $\log R(2) = 4.087$ for local galaxies is interpolated for the standards in Table 8. The surface brightness of $\langle \text{SB}_I(2) \rangle = 22.86$ mag/arcsec² at $\eta = 2.0$ is then spread to the η values of 1.0, 1.3, 1.5, and 1.7 using the surface brightness

ratios in the $n = 0.46$ column of Table 6. This procedure gives the standard $\langle \text{SB} \rangle, \eta$ curve for zero redshift at the five fiducial η values for local E galaxies.

The result for Cl 1324+3011 ($z = 0.7565$) is shown in Figure 8. The zero-redshift $\langle \text{SB} \rangle_I, \eta$ curves from Table 10, valid at the marked mean $R(\eta = 2)$ radii for each group, are shown in the upper part of the diagram. The data from Table 9 are plotted in the lower part for the three radius bins. The smooth curves are interpolated between the points. The bin number is marked at the left. Clearly, a Tolman signal is present. The family of observed curves is fainter than the family of zero-redshift calibration curves.

To see this signal more clearly, the data in each radius bin are plotted separately in Figure 9. Error bars are put on the observed points. Zero-redshift standard curves from Table 10, are shown as dashed. The shape of the Sérsic curve for $n = 0.46$ is brought down from the dashed curve near the top of each panel in Figure 9 and is zero-pointed to the data at $\eta = 1.5$.

The fit of *HST* data to the standard curve is excellent. The $\langle \text{SB} \rangle$ difference between the zero-redshift standard (upper curves) and the observed points is the effect we are seeking. It is the Tolman signal as modified by the luminosity change in the remote 1324 + 3011 cluster due to evolution in the look-back time.

The same analysis is made in Figures 10 & 11 for Cl 1604+4304 ($z = 0.8967$) from the data in Tables 11 & 12 (there are only two radius bins), and in Figures 12 & 13 for Cl 1604+4321 ($z = 0.9243$) from Tables 13 & 14.

The surface brightness differences between the remote and the local galaxies, read from Figures 9, 11, and 13, are collected in Table 15. The entries can be compared with Tables 5, 6, & 7 of LS01c. They are similar but not identical. The small difference between the studies is because the method of search here for the Tolman signal is not the same. There we accounted for the change of $\langle \text{SB} \rangle$ with intrinsic size by comparing the zero points of the $\langle \text{SB} \rangle, \text{radius}$ curve at *different* η values (Figs. 1 and 2 there). Here we compare the local and remote data at *fixed radii* as η is varied (Figs. 8–12 here). Part of the difference is also due to the slight change in the zero redshift standard $\langle \text{SB} \rangle$ - $\log R$ relation in Table 8. Each method uses the same observational data and with each we reach the same conclusion, which is this.

The differences in $\langle \text{SB} \rangle$ are large between remote and local galaxies over parts of E galaxy images defined by Petrosian η radii, but in each case are smaller than the $(1 + z)^4$ Tolman prediction. We interpret this to mean that a Tolman $(1 + z)^4$ cosmological signal exists but is degraded by luminosity evolution that amounts to approximately 0.8 mag in R and 0.4 mag in I . The exact values at the bottom of Table 15 are listed for each of the five

fiducial η positions in the mean of the E galaxy images for each radius bin.

6.1. The Estimated Errors

Before the error budget can be determined, two caveats are necessary.

(1) In Figures 8–13 we have used an $n = 0.46$ Sérsic exponent to define the shape of the zero redshift $\langle SB \rangle$ - η relation in every radius bin for the mean radius in each. However, following Binggeli & Jerjen (1998, their Fig. 2), we showed in Figures 6 & 7 using Tables 4 and 6 that the Sérsic n exponent is a strong function of the intrinsic $R(2)$ size. Hence, we should have used *different* standard zero-redshift curves with different n values that are relevant for the mean radius for each of the particular bins. We have ignored this detail because it makes a negligible difference in Table 15 and Figures 8–13.

Nevertheless it is of interest to estimate the variation of effective n values for the *HST* cluster galaxies. Figure 14 with Table 4 is useful in making the estimate. These show that, as the size varies between $\log R(2) = 3.5$ and 4.2, the Sérsic exponent varies between 0.4 and 0.6 for the *HST* galaxies. The mean over all the *HST* galaxies is $n = 0.46$, shown in Figure 15 from the data listed in Table 16.

(2) The second caveat is this. We have calculated the intrinsic sizes using a world model with $q_0 = 1/2$, $H_0 = 50$, $\Lambda = 0$. Different radii would be obtained for different q_0 models. Table 8 of LS01c shows that if $q_0 = 0$, the radii would be about 25% larger than we have used. If $q_0 = 1$, the R values would be 15% smaller. Therefore, using the slope of equation (9), the surface brightness of the standard zero redshift curves would be displaced relative to the *HST* points by 0.3 mag brighter and 0.18 mag fainter from the offsets we use here for $q_0 = 1/2$.

We have not calculated the effect on R using a finite value of Λ , taken from the current “concordance world model”, with assigned values of Λ and q_0 because the uncertainties here are at the level just stated for the range of q_0 from 0 to 1, and are bracketed by them.

This amounts to a *systematic* error over which we have no control unless we know the correct world model, which we do not. We ignore this systematic uncertainty in what follows, giving only the statistical errors for the $q_0 = 1/2$ case.

Ignoring these two caveats, the statistical errors are estimated as follows. We require the mean $\langle SB \rangle$ offsets in the $\langle SB \rangle$ vs. η curves between the zero redshift standard curves and the data points in Figures 9, 11, and 13. There are two components. (a) One is the difference between the observed points and the standard curves brought down from the zero

redshift $\langle \text{SB} \rangle$ curves. (b) The second is the accuracy with which we know the position of the standard curves at zero redshift for particular radius values.

(a). Table 15 lists the individual $\langle \text{SB} \rangle$ offsets for each fiducial η Petrosian homology position in each of the radius bins. The rms differences from the standard curves are small, averaging 0.06 mag for each cluster in each radius bin. In addition, there is no correlation of the residues with η , showing that the data have the same shape, on average, as the standard $n = 0.46$ Sérsic profile. The mean rms of the $\langle \text{SB} \rangle$ differences with the standard curve averages 0.12 mag over the range of η from 1.0 to 2.0. With five data points in each group, the average error of the offset is ± 0.06 mag.

(b). As read from the error in the least squares intercept in Table 2 of SL01, the accuracy with which we know the placement of the zero-redshift standard $\langle \text{SB} \rangle$ - η curve *at fixed radius* is ± 0.08 mag. However, the radius in each size bin itself varies within the bin, and its mean radius has an rms variation that also introduces a contribution to the placement error. These variations in $\langle R \rangle$ are listed within the body of Tables 9, 11, and 13. They average rms = 0.100, giving a mean error of ± 0.05 in $\log R$. From equation (9) this translates to an mean error in the placement of the standard SB curves at zero redshift of ± 0.15 mag. Adding this in quadrature to ± 0.08 mag gives a total mean placement error of the zero-redshift curves of ± 0.17 mag. Adding this in quadrature to the ± 0.06 mag mean error of the *HST* data points gives a total uncertainty of the mean $\langle \text{SB} \rangle$ offsets in Table 15 as ± 0.18 mag.

From Table 15 we adopt the mean $\langle \text{SB} \rangle$ offsets between the *HST* galaxies and the local E galaxies of the same size as 2.04 ± 0.18 mag for Cl 1324+3011 ($z = 0.7565$) in the rest frame *I* band, 2.51 ± 0.18 mag for Cl 1604+4304 ($z = 0.8967$) in the rest frame *I* band, and 1.99 ± 0.18 mag for Cl 1604+4321 ($z = 0.9243$) in the rest frame *R* band.

These offsets correspond to Tolman plus luminosity evolution signals of $p = 3.33 \pm 0.30$ for Cl 1324+3011 in the *I* band, $p = 3.61 \pm 0.26$ for Cl 1604+4304, also in the *I* band, and $p = 2.80 \pm 0.25$ for Cl 1604+4321 in the *R* band, where p is the exponent on $(1 + z)$. Combining the p values for the two clusters in the *I* band, and repeating the answer in the *R* band for Cl 1604+4321 gives the final answers as,

$$\Delta \langle \text{SB} \rangle = \begin{cases} 2.5 \log(1 + z)^{2.80 \pm 0.25} & \text{mag in the } R \text{ band} \\ 2.5 \log(1 + z)^{3.48 \pm 0.14} & \text{mag in the } I \text{ band.} \end{cases} \quad (10)$$

6.2. Evolution in the Look-Back Time

If the true Tolman signal is $(1+z)^4$, then the component due to luminosity evolution is $(1+z)^{4-p}$, which is,

$$M_{\text{evol}} = \begin{cases} 2.5 \log(1+z)^{1.20 \pm 0.25} & \text{mag in the } R \text{ band} \\ 2.5 \log(1+z)^{0.52 \pm 0.14} & \text{mag in the } I \text{ band.} \end{cases} \quad (11)$$

For redshifts of $z = 0.86$, which is the mean for the three *HST* clusters, these luminosity evolutions are 0.81 mag in rest frame *R* and 0.35 mag in rest frame *I*. Such luminosity changes at this mean redshift are consistent with the stellar evolution models of Bruzual & Charlot (1993) if the initial star formation was a burst near the beginning of the creation of the galaxy (LS01c, § 4.2). Equations (10) and (11) are closely the same as Lubin and I (LS01c) found, using a different representation of the *HST* data.

Q.E.D.

I have been told by my son John, who majored in physics at University of California, Davis that the professor of advanced mechanics would post the solutions to the weekly five assigned problems a week after they were due, and always signed the solutions Q.E.D. As the difficulty of the problems increased week by week, some of the students grew increasingly disturbed by what they conceived to be a mocking by the professor, because they thought that Q.E.D. meant “Quite Easily Done” rather than “Quod Erat Demonstrandum”, meaning “As Was To Be Demonstrated”.

The solution of the Tolman test given by LS01c and differently here has not been quite as easily done as I set out at the planning meeting for the *LST* in 1974. It has required many developments not yet made at the time. However, the test seems to have been successful. The Tolman prediction is verified. The expansion would seem to be real.

7. SUMMARY AND DISCUSSION

7.1. Preliminaries

One of the major problems that hampered progress was how to define a homologous radius at which to compare the surface brightness of local and remote E galaxies. An obvious early choice was the half-light radius r_e , but this was hard to measure before the advent of area detectors. To determine r_e requires a growth curve that extends to “infinite” radius so

that it can be backed off by 0.75 mag to the half-light value. Finding the asymptotic “total” magnitude depends on an assumed luminosity profile which is generally not the standard de Vaucouleurs $r^{1/4}$ curve.

Another scale-free radius is the Hubble a fitting parameter, used in my first proposal for the test with an *LST*. This is the radius where the measured surface brightness is 1/4 of the central value. However, this is even harder to measure. It requires knowing the central intensity, which is elusive because of insufficient spatial resolution of the telescope, the detector, and from the ground, the seeing.

The solution has been to use Petrosian radii, defined as the comparison of the SB at a particular radius to the average surface brightness, $\langle SB \rangle$, inside that radius. We have formulated the Tolman test, both in SP90a,b, LS01a,b,c and here by using Petrosian radii throughout.

The properties of various ratios of measurable parameters at Petrosian η values of 1.0, 1.3, 1.5, 1.7, and 2.0 mag is the subject of § 3. The two diagnostic diagrams of Figures 3 & 5 are central to the discussion. They are related to the luminosity profile, permitting the assigning of a particular Sérsic profile to the data but also providing a way to calculate the $\langle SB \rangle$ over a range of η radii when the $\langle SB \rangle$ is known at $\log R$ at $\eta = 2$. Based on these two diagrams, we have used 11 steps to complete the Tolman test.

7.2. The Eleven Steps

Only the shape of the $\langle SB \rangle$ vs. η standard curve is given by the second diagnostic diagram in Figure 5. Once the Sérsic n exponent is known, the shape of its standard curve must be calibrated in zero point. We proceed in eight steps for this calibration.

(1). By the method in § 5 we determine the zero point of the $\langle SB \rangle$ vs. $\log R$ zero redshift curve at the R radius corresponding to $\eta = 2.0$. The results are in equations (6)–(9) in the V and R_{cape} band passes, valid for $\log R > 4.3$.

(2). For smaller radii, non-linear corrections to these equations have been determined from photometric data in the Virgo, Fornax, & Coma clusters. These are listed in Table 7.

(3). Applying Table 7 to equation (9) gives the $\langle SB \rangle$ averaged over R at zero redshift vs. the $\log R$ values in Table 8, tabulated in V , R , and I for intrinsic radii at $\eta = 2.0$ over the range of $\log R$ from 5.4 to 3.4 (pc).

(4). The calibration of $\langle SB \rangle$ vs. R at η values other than 2.0 is found by spreading the

calibration of Table 7 to the four fiducial η values between 2.0 to 1.0 by using the diagnostic diagram of Figure 5 (Table 6) with a Sérsic exponent of $n = 0.46$, determined as follows.

(5). Proof that the Sérsic family of profiles is appropriate and that the correct Sérsic n exponent can be found is made by recovering the discovery, made by the many authors cited, that n varies strongly with absolute magnitude. From Figures 7 and 8 in § 4, it is shown that both the $\log r(\eta = 1)/r(2)$ radii ratios in Figure 3 and the $\langle \text{SB}(2) \rangle - \langle \text{SB}(1) \rangle$ differences in Figure 5 vary systematically with $\log R$. That this must be so, provided that the Sérsic family is a good fit to E galaxy profiles, follows from the discovery by Binggeli & Jerjen (1998) that the Sérsic n exponent varies between 0.15 and 1.5 as the absolute magnitude of E galaxies becomes fainter between $M_B = -23$ and -13 for Virgo cluster galaxies.

(6). Reading Figure 6 at $\log R = 3.9$, which is the average for galaxies in the in the *HST* sample, and interpolating with $\langle \log r(1)/r(2) \rangle = -0.50$ between the Sérsic n values, gives $n = 0.46$.

(7). Reading Table 6 at this n gives the $\langle \text{SB} \rangle$ differences with $\langle \text{SB}(\eta = 2.0) \rangle$ needed to spread the calibration from $\eta = 2$ to the other four fiducial η values we are using.

(8). This calibration of the $\langle \text{SB} \rangle$ - $\log R$ relation for local E galaxies at zero redshift at these five η values at the mean radii of the size bins used for the *HST* clusters is listed in Tables 10, 12, & 14 of § 6.

This completes the calibration steps. The remaining steps to the Tolman test itself are three.

(9). Figures 8–13 show the comparison of the $\langle \text{SB} \rangle$ of local E galaxies with the three *HST* clusters, broken into radius bins to compensate for the variation of $\langle \text{SB} \rangle$ with intrinsic radii. The Tolman signals, degraded by luminosity evolution, are listed in Table 15. The errors are put at ± 0.18 mag in each radius bin by the accounting in § 6.1.

(10). Equations (10) and (11) divide the observed data between a Tolman $(1+z)^4$ signal and that portion due to luminosity evolution.

(11). That a Sérsic profile with $n = 0.46$ is appropriate for the local standards and for the three *HST* cluster galaxies at these absolute magnitudes, is shown in Figures 6, 7 & 15, using Tables 4 & 16.

The two conclusions are that the universe expands, and that there is luminosity evolution in the look-back time. Although Q.E.D., it has not been quite so easily done as the way we tried to sell it for the *LST* in 1974.

I am grateful to G. A. Tammann for reading an early draft of the paper and for making comments that have clarified a number of the arguments. Bernd Reindl's skill is greatly appreciated in preparing the diagrams in digital form, and in preparing the text in the proper format with dispatch. John Grula, editorial chief for the Observatories, formed again the liaison with the press, for which I am grateful. I thank the Carnegie Institution for its support with post retirement facilities and publication charges.

REFERENCES

- Binggeli, B., & Jerjen H. 1998, *A&A*, 333, 17
- Binggeli, B., Sandage, A., & Tarenghi, M. 1984, *AJ*, 89, 64
- Bruzual, A. G., & Charlot, S. 1993, *ApJ*, 405, 538
- Burbidge, E. M., Burbidge, G. R., & Crampin, D. J. 1964, *ApJ*, 140, 1462
- Caldwell, N. 1987, *AJ*, 94, 1116
- Caldwell, N., & Bothun, G. 1987, *AJ*, 94, 1126
- Caon, N., Capaccioli, M., & D'Onofrio, M. 1993, *MNRAS*, 265, 1013
- Choloniewski, J. 1985, *MNRAS*, 214, 197
- Code, A., & Welch, G. A. 1979, *ApJ*, 228, 95
- Coleman, G. D., Wu, C.-C., & Weedman, D. W. 1980, *ApJS*, 43, 393
- de Vaucouleurs, A., & Longo, G. 1988, *Catalogue of Visual and Infrared Photometry of Galaxies from 0.5 μm to 10 μm* (Austin: Univ. of Texas)
- de Vaucouleurs, G., de Vaucouleurs, A., Corwin, H. G., Buta, R. J., Paturel, G., & Fouqué, P. 1991, *Third Reference Catalogue of Bright Galaxies* (New York: Springer) (RC3)
- Djorgovski, S., & Davis, M. 1987, *ApJ*, 313, 59
- Djorgovski, S. B., & Spinrad, H. 1981, *ApJ*, 251, 417
- Ferguson, H. C., & Sandage, A. 1988, *AJ*, 96, 1520
- Fraser, C. W. 1977, *A&AS*, 29, 161
- Greenstein, J. L. 1938, *ApJ*, 88, 605

- Hodge, P. M. 1978, ApJS, 37, 429
- Hubble, E. 1934, ApJ, 79, 8
- Hubble, E. 1936, ApJ, 84, 517
- Hubble, E. 1937, *The Observational Approach to Cosmology* (Oxford: Clarendon Press)
- Hubble E. 1953, MNRAS, 113, 658, *The Darwin Lecture*
- Hubble, E., & Tolman, R. C. 1935, ApJ, 82, 302
- Ichikawa, S.-I., Wakamatsu, K.-I., & Okamura, S. 1986, ApJS, 60, 475
- Impey, C., Bothun, G. & Malin, D. 1988, ApJ, 330, 634
- Jedrzejewski, R. 1987, MNRAS, 226, 747
- Johnson, H. L. 1965, ApJ, 141, 170
- King, I. 1978, ApJ, 222, 1
- Kormendy, J. 1977, ApJ, 218, 333
- Kormendy, J. 1987, in *Nearly Normal Galaxies: From the Planck time to the present*, ed. S. Faber (New York: Springer), 163
- Kormendy, J., Fisher, D. B., Cornell, M. E., & Bender, R. 2009, ApJS, 182, 216
- Kron, R. G. 1995, in *Saas-Fee Advanced Course 23, The Deep Universe*, ed. B. Binggeli & R. Buser (Berlin: Springer), 233
- Landolt, A. 1983, AJ 88, 489 (UBVRI)
- Landolt, A. 1992, AJ, 104, 340 (UBVRI)
- Lubin, L. M., Postman, M., Oke, J. B., Ratnatunga, K. U., Gunn, J. E., Hoessel, J. G., & Schneider, D. P. 1998, AJ, 116, 584
- Lubin, L. M., Postman, M., Oke, J. B., Brunner, R., Gunn, J. E., & Schneider, D. 2001, AJ, said to be in preparation
- Lubin, L. M., & Sandage, A. 2001a, AJ, 121, 2289 (LS01a), Paper II
- Lubin, L. M., & Sandage, A. 2001b, AJ, 122, 1071, (LS01b), Paper III

- Lubin, L. M., & Sandage, A. 2001c, AJ, 122, 1084, (LS01c), Paper IV
- Malumuth, E. M., & Kirshner, R. P. 1985, ApJ, 291, 8
- Mattig, W. 1958, Astron. Nachr., 284, 109
- Michard, R. 1979, A&A, 74, 206
- Molaro, P., Levshakov, S. A., Dessauges-Zavadsky, M., & D’Odorico, S. 2002, A&A, 381, L64
- Oberth, H. 1923, Die Rakete zu den Planetenräumen (München: Oldenbourg Verlag)
- Oemler, A. 1973, Ph.D. thesis, California Institute of Technology
- Oemler, A. 1974, ApJ, 194, 1
- Oemler, A. 1976, ApJ, 209, 693
- Oke, J. B., Postman, M., & Lubin, L. M. 1998, AJ, 116, 549 (OPL 1998)
- Oke, J. B., & Sandage, A. 1968, ApJ, 154, 21
- Pence, W. 1976, ApJ, 203, 39
- Petrosian, V. 1976, ApJ, 209, L1
- Postman, M., & Lauer, T. 1995, ApJ, 440, 28 (PL95)
- Postman, M., Lubin, L., & Oke, J. B. 1998, AJ, 116, 560 (PLO 1998)
- Postman, M., Lubin, L., & Oke, J. B. 2001, AJ, 122, 1125 (PLO 2001)
- Poulain, P., & Nieto, J-L. 1994, A&AS, 103, 573
- Sandage, A. 1961, ApJ, 133, 355
- Sandage, A. 1968, in Galaxies and the Universe, ed. L. Woltjer (New York: Columbia Univ. Press), 75
- Sandage, A. 1972, ApJ, 173, 485
- Sandage, A. 1973, ApJ, 183, 731
- Sandage, A. 1974, in Large Space Telescope – A New Tool For Science, ed. P. F. Simmons (New York: AIAA), 19

- Sandage, A. 1988, *ARA&A*, 26, 561
- Sandage, A. 1995, in *Saas-Fee Advanced Course 23, The Deep Universe*, ed. B. Binggeli & R. Buser (Berlin: Springer), 1
- Sandage, A. 1997, *PASP*, 109, 1193
- Sandage, A. 1998, in *STScI Symp. 11, The Hubble Deep Field*, ed. M. Livio, S. M. Fall, & P. Madau (New York: Cambridge Univ. Press), 1
- Sandage, A. 2001, *PASP*, 113, 267
- Sandage, A., & Lubin, L. M. 2001, *AJ*, 121, 2271 (SL01), Paper I
- Sandage, A., & Perelmuter, J.-M. 1990a, *ApJ*, 350, 481 (SP90a)
- Sandage, A., & Perelmuter, J.-M. 1990b, *ApJ*, 361, 1 (SP90b)
- Sandage, A., & Perelmuter, J.-M. 1991, *ApJ*, 370, 455 (SP91)
- Sandage, A., & Smith, L. L. 1963, *ApJ*, 137, 1057
- Schild, R., & Oke, J. B. 1971, *ApJ*, 169, 209
- Schombert, J. M. 1986, *ApJS*, 60, 603
- Schombert, J. M. 1987, *ApJS*, 64, 643
- Seares, F. H., Kapteyn, J. C., & van Rhijn, P. J. 1930, *The Mount Wilson Catalogue of Photographic Magnitudes in Selected Areas 1-39*, Publ. 402 (Washington: Carnegie Inst. of Washington)
- Sérsic, J.-L. 1968, *Atlas de Galaxias Australes* (Córdoba: Obs. Astron.)
- Songaila, A., et al. 1994, *Nature*, 371, 43
- Spitzer, L. 1946, RAND project report, reprinted in *Astron. Quart.*, 7, 131 (1990)
- Srianand, R., Petitjean, P., & Ledoux, C. 2000, *Nature*, 408, 931
- Stebbins, J., Whitford, A. E., & Johnson, H. L. 1950, *ApJ*, 112, 469
- Strom, K. M., & Strom, S. E. 1978a, *AJ*, 83, 73
- Strom, K. M., & Strom, S. E. 1978c, *AJ*, 83, 1293

- Strom, S. E., & Strom, K. M. 1978b, *AJ*, 83, 732
- Thomsen, B. & Frandsen, S. 1983, *AJ*, 88, 789
- Thuan, T. X., & Romanishin, W. 1981, *ApJ*, 248, 439
- Tolman, R. C. 1930, *Proc. Nat. Acad. Sci.*, 16, 511
- Tolman, R. C. 1934, *Relativity, Thermodynamics, & Cosmology* (Oxford: Clarendon Press), 467
- Vigroux, L., Souviron, J., Lachieze-Rey, M., & Vader, J. P. 1988, *A&AS*, 73, 1
- Wells, D. C. 1973, Ph.D. thesis, Univ. of Texas at Austin
- Whitford, A. E. 1971, *ApJ*, 169, 215
- Yoshii, Y., & Takahara, F. 1988, *ApJ*, 326, 1

Table 1. Growth-Curve Magnitudes and Petrosian η Radii as Function of $\log r/r_e$ For Various Hubble Types and for the de Vaucouleurs $r^{1/4}$ law.

$\log r/r_e$	$T = -5 : E$		Sérsic $n = 0.25$		$T = 1 : Sa$		Sérsic $n = 0.46$		$T = 3 : Sb$		$T = 5 : Sc$		$T = 7 : Sd$		$T = 9 : Sm$	
	Δm	η	Δm	η	Δm	η	Δm	η	Δm	η	Δm	η	Δm	η	Δm	η
	(1)	(2)	(3)	(4)	(5)	(6)	(7)	(8)	(9)	(10)	(11)	(12)	(13)	(14)	(15)	(16)
-1.0	2.97	...			3.22	...			3.41	...	3.65	...	3.99	...	4.43	...
-0.9	2.69	0.65	2.70	0.61	2.95	0.67	3.45	0.36	3.13	0.61	3.33	0.54	3.63	0.39	4.01	0.22
-0.8	2.42	0.69	2.36	0.77	2.68	0.61	3.00	0.40	2.84	0.59	3.04	0.59	3.29	0.48	3.61	0.27
-0.7	2.16	0.73	2.04	0.83	2.38	0.61	2.62	0.44	2.55	0.67	2.77	0.67	2.99	0.57	3.23	0.34
-0.6	1.91	0.80	1.80	0.89	2.11	0.73	2.30	0.49	2.30	0.71	2.50	0.59	2.70	0.47	2.88	0.28
-0.5	1.68	0.89	1.61	0.97	1.87	0.75	2.00	0.55	2.03	0.65	2.19	0.56	2.34	0.40	2.46	0.27
-0.4	1.47	0.94	1.41	1.03	1.61	0.80	1.69	0.62	1.75	0.69	1.90	0.57	2.01	0.47	2.10	0.34
-0.3	1.26	1.02	1.23	1.10	1.39	0.92	1.42	0.72	1.50	0.73	1.60	0.56	1.68	0.45	1.73	0.34
-0.2	1.08	1.14	1.06	1.19	1.18	0.92	1.21	0.82	1.24	0.73	1.30	0.59	1.35	0.48	1.37	0.42
-0.1	0.91	1.20	0.90	1.28	0.96	0.92	0.92	0.94	0.99	0.78	1.02	0.65	1.04	0.65	1.05	0.52
0.0	0.75	1.31	0.75	1.39	0.75	0.89	0.74	1.08	0.75	0.89	0.75	0.73	0.75	0.69	0.75	0.65
0.1	0.61	1.46	0.64	1.50	0.57	1.14	0.60	1.23	0.55	1.05	0.53	1.00	0.51	0.94	0.50	0.89
0.2	0.49	1.64	0.50	1.63	0.40	1.38	0.45	1.41	0.37	1.31	0.35	1.27	0.33	1.31	0.31	1.27
0.3	0.39	1.80	0.41	1.80	0.29	1.69	0.31	1.61	0.25	1.64	0.22	1.60	0.21	1.60	0.19	1.64
0.4	0.30	1.99	0.32	1.97	0.19	1.92	0.22	1.87	0.15	1.99	0.12	2.06	0.10	2.06	0.09	2.14
0.5	0.23	2.12	0.25	2.14	0.12	2.22	0.15	2.19	0.09	2.40	0.07	2.61	0.06	2.89	0.05	2.89
0.6	0.17	2.50	0.18	2.38	0.06	2.89	0.09	2.58	0.04	3.06	0.03	3.25	0.03	3.25	0.02	3.50
0.7	0.13	2.24	0.14	2.60	0.05	3.81	0.03	3.00	0.03	4.25	0.02	4.25	0.01	3.81	0.01	4.25
0.8	0.09	2.89	0.10	2.90	0.03	3.50	0.01	3.52	0.02	...	0.01	...	0.01	4.25		
0.9	0.06	3.25	0.07	3.27	0.01	4.25	0.00	4.20	0.01	...						
1.0	0.04	3.81	0.05	3.70	0.00	...										

Table 2. Calculated b_n Values for the Sérsic Family of Luminosity Profiles.

Sérsic n	b_n	Sérsic n	b_n
(1)	(2)	(3)	(4)
0.15	5.62	0.46	1.72
0.20	4.17	0.60	1.28
0.25	3.33	1.00	0.73
0.40	2.00	1.50	0.44

Table 3. Growth Curves and η Values for the Sérsic Function at the Listed $\log r/r_e$ Ratios.

$\log r/r_e$ (1)	$n = 0.15$		$n = 0.20$		$n = 0.25$		$n = 0.40$		$n = 0.46$		$n = 0.60$		$n = 1.00$		$n = 1.50$	
	Δm (2)	η (3)	Δm (4)	η (5)	Δm (6)	η (7)	Δm (8)	η (9)	Δm (10)	η (11)	Δm (12)	η (13)	Δm (14)	η (15)	Δm (16)	η (17)
-0.4	1.26	1.26	1.34	1.13	1.41	1.03	1.60	0.74			1.79	...	2.05	...	2.30	...
-0.3	1.14	1.35	1.19	1.20	1.23	1.10	1.32	0.80			1.55	...	1.70	...	1.81	...
-0.2	1.00	1.41	1.02	1.29	1.06	1.19	1.10	0.88	1.18	0.82	1.28	0.66	1.40	0.40	1.42	0.21
-0.1	0.86	1.51	0.89	1.38	0.90	1.28	0.94	1.00	0.92	0.94	1.00	0.76	1.05	0.54	1.08	0.32
0.0	0.75	1.60	0.75	1.47	0.75	1.39	0.75	1.14	0.74	1.08	0.75	0.90	0.75	0.72	0.75	0.50
0.1	0.64	1.70	0.63	1.60	0.64	1.50	0.61	1.26	0.59	1.23	0.55	1.10	0.50	0.94	0.44	0.73
0.2	0.56	1.80	0.52	1.71	0.50	1.63	0.48	1.44	0.45	1.41	0.38	1.30	0.32	1.20	0.25	1.06
0.3	0.48	1.91	0.43	1.88	0.41	1.80	0.33	1.63	0.31	1.61	0.26	1.56	0.20	1.52	0.11	1.53
0.4	0.40	2.08	0.36	2.01	0.32	1.97	0.22	1.86	0.22	1.87	0.15	1.90	0.11	2.10	0.04	2.36
0.5	0.33	2.19	0.29	2.19	0.25	2.14	0.16	2.14	0.15	2.19	0.08	2.31	0.04	2.80	0.01	4.10
0.6	0.27	2.32	0.21	2.37	0.18	2.38	0.10	2.43	0.09	2.58	0.03	2.80	0.00	3.91		
0.7	0.21	2.51	0.16	2.53	0.14	2.60	0.06	2.80	0.03	3.00	0.00	3.38				
0.8	0.15	2.67	0.11	2.77	0.10	2.90	0.04	3.24	0.01	3.52						
0.9	0.11	2.88	0.09	2.99	0.07	3.27	0.02	3.75	0.00	4.20						
1.0	0.07	3.10	0.04	3.23	0.05	3.70	0.00	...								
1.1	0.05	3.32	0.02	3.53	0.03	...	0.00	...								
1.2	0.02	3.50	0.01	3.88												

Table 4. $\log r/r(\eta = 2)$ at Various η Values for the Sérsic Family from Table 3.

η/n	0.15	0.20	0.25	$T = -5$	0.40	0.46	0.60	1.00	1.50
(1)	(2)	(3)	(4)	(5)	(6)	(7)	(8)	(9)	(10)
1.0	...	(-1.0)	-0.82	-0.72	-0.65	-0.50	-0.34	-0.27	-0.15
1.3	-0.78	-0.58	-0.51	-0.42	-0.31	-0.29	-0.21	-0.15	-0.10
1.5	-0.51	-0.38	-0.32	-0.28	-0.21	-0.18	-0.14	-0.09	-0.06
1.7	-0.29	-0.21	-0.20	-0.16	-0.11	-0.10	-0.06	-0.06	-0.03
2.0	0.00	0.00	0.00	0.00	0.00	0.00	0.00	0.00	0.00
2.5	0.33	0.28	0.22	0.21	0.17	0.15	0.09	0.07	0.05
3.0	0.59	0.50	0.41	0.40	0.28	0.26	0.18	0.13	0.09
3.5	0.81	0.70	0.56	0.54	0.40	0.36	0.26	0.19	0.13
4.0	...	0.83	0.69	0.62	0.50	0.44	0.30	0.22	0.17

Table 5. $\log r/r(\eta = 2)$ as Function of η and the α -to- β Ratio for Four Oemler Profiles and the Observed $T = -5$ and a Sérsic Profile With $n = 0.46$.

η	α -to- β Ratio				E	Sérsic
	10	30	60	100	$T = -5$	0.46
(1)	(2)	(3)	(4)	(5)	(6)	(7)
1.0	-0.44	-0.70	-0.88	-0.91	-0.72	-0.50
1.3	-0.25	-0.42	-0.58	-0.67	-0.42	-0.29
1.5	-0.18	-0.26	-0.38	-0.46	-0.28	-0.18
1.7	-0.10	-0.14	-0.21	-0.25	-0.16	-0.10
2.0	0.00	0.00	0.00	0.00	0.00	0.00
2.5	0.10	0.15	0.20	0.26	0.21	0.15
3.0	0.18	0.24	0.31	0.40	0.40	0.26
3.5	0.22	0.31	0.39	0.48	0.54	0.36

Table 6. Surface Brightness Normalized to $\eta = 2$ for Eight Sérsic Profiles, Averaged Over the Area Interior to the Listed η Radii. The Unit is Magnitudes (Relative to $\eta = 2$ Values) Per Unit Area.

η/n	0.15	0.20	0.25	$T = -5^a$	0.40	0.46	0.60	1.00	1.50
(1)	(2)	(3)	(4)	(5)	(6)	(7)	(8)	(9)	(10)
1.0	...	-3.30	-2.82	-2.78	-2.02	-1.70	-1.38	-0.93	-0.52
1.3	...	-2.15	-1.82	-1.78	-1.18	-1.10	-0.83	-0.58	-0.35
1.5	-1.80	-1.50	-1.20	-1.25	-0.78	-0.73	-0.60	-0.38	-0.26
1.7	-1.07	-0.85	-0.68	-0.73	-0.48	-0.40	-0.38	-0.20	-0.14
2.0	0.00	0.00	0.00	0.00	0.00	0.00	0.00	0.00	0.00
2.5	1.52	1.37	1.10	0.97	0.68	0.64	0.48	0.32	0.25
3.0	2.66	2.45	1.90	1.58	1.30	1.25	1.13	0.59	0.46
3.5	3.62	3.30	2.60	2.20	1.85	1.72	1.54	0.80	0.66
4.0	...	3.90	...	2.72	2.30	2.21	2.05	1.00	0.84

^aCalculated from the observed $T = -5$ growth curve.

Table 7. Nonlinear Corrections to Equations (6)–(9).^a

$\log R$	$\Delta\langle\text{SB}\rangle$ (mag)	$\log R$	$\Delta\langle\text{SB}\rangle$ (mag)
(1)	(2)	(3)	(4)
4.4	0.00	3.8	0.42
4.3	0.02	3.7	0.50
4.2	0.06	3.6	0.60
4.1	0.10	3.5	0.67
4.0	0.23	3.4	0.75
3.9	0.36	3.3	0.86

^aThe R radii are based on distance moduli of 31.7 for Virgo, 31.9 for Fornax, and 35.5 for Coma.

Table 8. Ridge-Line Variation of $\langle\text{SB}\rangle$ with the $\log R$ Intrinsic Size at $\eta = 2$ at Zero Redshift for E Galaxies in the $V(RI)_{\text{cape}}$ Pass Bands.^{a,b}

$\log R(2)$	$\langle\text{SB}\rangle_V$	$\langle\text{SB}\rangle_R$	$\langle\text{SB}\rangle_I$
(1)	(2)	(3)	(4)
5.4	25.14	24.57	23.93
5.2	24.56	23.99	23.35
5.0	23.95	23.38	22.74
4.8	23.36	22.79	22.15
4.6	22.76	22.19	21.55
4.4	22.17	21.60	20.96
4.2	21.63	21.06	20.42
4.0	21.21	20.64	20.00
3.8	20.81	20.24	19.60
3.6	20.39	19.82	19.18
3.4	19.95	19.38	18.74

^aThe entries are calculated from equation (9) using the nonlinear corrections of Table 7.

^bThe unit of the $\langle\text{SB}\rangle$ entries is $\text{mag}(\text{arc sec})^{-2}$.

Table 9. *HST* $\langle \text{SB} \rangle$ Data For a Range of η Values for Cl 1324+3011 Binned Into Three Radius Groups.

Item/ η	1.0	1.3	1.5	1.7	2.0
(1)	(2)	(3)	(4)	(5)	(6)
<i>Group 1</i> $n = 2$ $\langle M_I \rangle_{\eta=2} = -23.49$					
$\langle \text{SB} \rangle_I$	20.17	21.28	21.88	22.42	22.86
error	± 0.39	± 0.22	± 0.14	± 0.26	± 0.33
$\langle \log R \rangle$	3.487	3.815	3.911	4.061	4.087
rms	0.060	0.126	0.218	0.124	0.080
<i>Group 2</i> $n = 6$ $\langle M_I \rangle_{\eta=2} = -22.98$					
$\langle \text{SB} \rangle_I$	19.95	20.61	20.99	21.34	21.77
error	± 0.24	± 0.15	± 0.10	± 0.08	± 0.09
$\langle \log R \rangle$	3.424	3.608	3.708	3.797	3.898
rms	0.159	0.125	0.111	0.112	0.117
<i>Group 3</i> $n = 5$ $\langle M_I \rangle_{\eta=2} = -22.01$					
$\langle \text{SB} \rangle_I$	19.48	20.03	20.31	20.55	20.88
error	± 0.35	± 0.38	± 0.37	± 0.37	± 0.39
$\langle \log R \rangle$	3.177	3.326	3.396	3.454	3.530
rms	0.096	0.098	0.098	0.102	0.106
<i>Grand mean</i> $n = 13$ $\langle M_I \rangle_{\eta=2} = -23.03$					
$\langle \text{SB} \rangle_I$	19.97	20.78	21.23	21.57	21.91
error	± 0.18	± 0.17	± 0.18	± 0.22	± 0.24
$\langle \log R \rangle$	3.410	3.644	3.769	3.827	3.883
rms	0.155	0.206	0.260	0.238	0.216

Table 10. Zero Redshift Surface Brightness - η Relation For a Sérsic Profile With $n = 0.46$ at the Mean $\log R(2)$ for the Three Radius Groups for *HST* Cl 1324+3011.^{a,b}

$\eta/\langle \log R \rangle$	4.087	3.898	3.530	3.882
(1)	(2)	(3)	(4)	(5)
1.0	18.48	18.08	17.30	18.01
1.3	19.08	18.68	17.90	18.61
1.5	19.45	19.05	18.27	18.98
1.7	19.78	19.38	18.60	19.31
2.0	20.18	19.78	19.00	19.71
	G1	G2	G3	mean

^aThe listed values are the surface brightness averaged over the area interior to the listed η radii.

^bThe units for the surface brightness are mag per (arc sec)² in the Cape *I* band.

Table 11. Same as Table 9 for *HST* Cl 1604+4304 ($z = 0.8967$).

Item/ η	1.0	1.3	1.5	1.7	2.0
(1)	(2)	(3)	(4)	(5)	(6)
<i>Group 1</i> $n = 3/4$ $\langle M_I \rangle_{\eta=2} = -23.09$					
$\langle \text{SB} \rangle_I$	20.89	21.70	22.16	22.47	22.86
error	± 0.13	± 0.08	± 0.11	± 0.11	± 0.32
$\langle \log R \rangle$	3.578	3.816	3.940	4.016	4.070
rms	0.106	0.156	0.141	0.145	0.137
<i>Group 2</i> $n = 3$ $\langle M_I \rangle_{\eta=2} = -22.79$					
$\langle \text{SB} \rangle_I$	20.35	20.84	21.11	21.40	21.82
error	± 0.23	± 0.22	± 0.20	± 0.19	± 0.18
$\langle \log R \rangle$	3.425	3.560	3.635	3.705	3.803
rms	0.087	0.094	0.097	0.102	0.106
<i>Grand mean</i> $n = 6$ $\langle M_I \rangle_{\eta=2} = -22.94$					
$\langle \text{SB} \rangle_I$	20.66	21.33	21.71	22.01	22.34
error	± 0.16	± 0.21	± 0.24	± 0.25	± 0.29
$\langle \log R \rangle$	3.512	3.706	3.809	3.883	3.937
rms	0.122	0.184	0.199	0.204	0.183

Table 12. Standard η -Surface Brightness Curves at Zero Redshift for the Two Radius Bins for *HST* Cl 1604+4304 and for Four Arbitrary Bins for Illustration.

$\eta/\langle \log R \rangle$	4.070	3.803	3.937	3.50	4.00	4.50	5.00
(1)	(2)	(3)	(4)	(5)	(6)	(7)	(8)
1.0	18.40	17.88	18.22	17.35	18.30	19.55	21.02
1.3	19.00	18.48	18.82	17.95	18.90	20.15	21.62
1.5	19.37	18.85	19.19	18.32	19.27	20.52	21.99
1.7	19.70	19.18	19.52	18.65	19.60	20.85	22.32
2.0	20.10	19.58	19.92	19.05	20.00	21.25	22.72
	G1	G2	mean				

Table 13. Same as Tables 9 and 11 but for *HST* Cl 1604+4321.

Item/ η	1.0	1.3	1.5	1.7	2.0
(1)	(2)	(3)	(4)	(5)	(6)
<i>Group 1</i> $n = 3$ $\langle M_R \rangle_{\eta=2} = -22.95$					
$\langle \text{SB} \rangle_R$	21.03	21.79	22.28	22.78	23.22
error	± 0.45	± 0.49	± 0.48	± 0.38	± 0.27
$\langle \log R \rangle$	3.611	3.741	3.872	4.001	4.104
rms	0.035	0.175	0.161	0.115	0.059
<i>Group 2</i> $n = 7$ $\langle M_R \rangle_{\eta=2} = -22.64$					
$\langle \text{SB} \rangle_R$	20.49	21.21	21.55	21.92	22.40
error	± 0.15	± 0.18	± 0.18	± 0.19	± 0.16
$\langle \log R \rangle$	3.378	3.583	3.672	3.763	3.885
rms	0.109	0.075	0.081	0.072	0.078
<i>Group 3</i> $n = 2$ $\langle M_R \rangle_{\eta=2} = -22.26$					
$\langle \text{SB} \rangle_R$	20.05	20.69	21.00	21.32	21.77
error	± 0.31	± 0.35	± 0.37	± 0.43	± 0.49
$\langle \log R \rangle$	3.249	3.412	3.496	3.379	3.667
rms	0.042	0.044	0.027	0.016	0.000
<i>Grand mean</i> $n = 12/14$ $\langle M_R \rangle_{\eta=2} = -22.65$					
$\langle \text{SB} \rangle_R$	20.60	21.31	21.69	22.08	22.50
error	± 0.15	± 0.17	± 0.18	± 0.19	± 0.18
$\langle \log R \rangle$	3.394	3.594	3.692	3.789	3.890
rms	0.146	0.151	0.163	0.168	0.160

Table 14. Same as Tables 10 & 12 but for Cl 1604+4321.

$\eta/\langle \log R \rangle$	4.104	3.885	3.667	3.904
(1)	(2)	(3)	(4)	(5)
1.0	19.16	18.64	18.27	18.74
1.3	19.76	19.24	18.87	19.34
1.5	20.13	19.61	19.24	19.71
1.7	20.44	19.92	19.57	20.04
2.0	20.84	20.32	19.97	20.44
	G1	G2	G3	mean

Table 15. Difference in the Surface Brightness Between the *HST* Clusters and the Zero Redshift Standard SB vs. η Curves for Each of the Radius Bins at Each of the Fiducial η Values.^a

η	Cl 1324+3011			$\Delta \langle \text{SB} \rangle_I$ (mag)		Cl 1604+4321		
	in I_{cape}			Cl 1604+4304		in R_{cape}		
	G1	G2	G3	G1	G2	G1	G2	G3
(1)	(2)	(3)	(4)	(5)	(6)	(7)	(8)	(9)
1.0	1.69	1.87	1.96	2.49	2.47	1.87	1.85	1.78
1.3	2.20	1.93	2.13	2.70	2.36	2.03	1.97	1.82
1.5	2.43	1.94	2.04	2.79	2.26	2.16	1.94	1.76
1.7	2.64	1.96	1.88	2.76	2.24	2.34	2.00	1.75
2.0	2.68	1.99	1.88	2.76	2.24	2.38	2.08	1.80
n	2	6	5	3	3	3	7	2
wt mean (mag)		2.04			2.51		1.99	
$(1+z)^4$ (mag)		2.45			2.78		2.84	

^aThe listings are the Tolman signal (in mags), degraded by luminosity evolution in the look-back time.

Table 16. Average $\log r(\eta)/r(2)$ vs. η Listed Separately for Each of the *HST* Clusters and the Average Over All *HST* Galaxies. The Mean Values Are Shown in Figure 15.

Cluster/ η	$\langle \log r(\eta)/r(2) \rangle$					n
	1.0	1.3	1.5	1.7	2.0	
(1)	(2)	(3)	(4)	(5)	(6)	(7)
1324+3011	-0.489	-0.291	-0.195	-0.091	0.000	11
1604+4304	-0.454	-0.273	-0.169	-0.096	0.000	6
1604+4321	-0.510	-0.310	-0.213	-0.115	0.000	13
mean	-0.491	-0.296	-0.198	-0.102	0.000	30

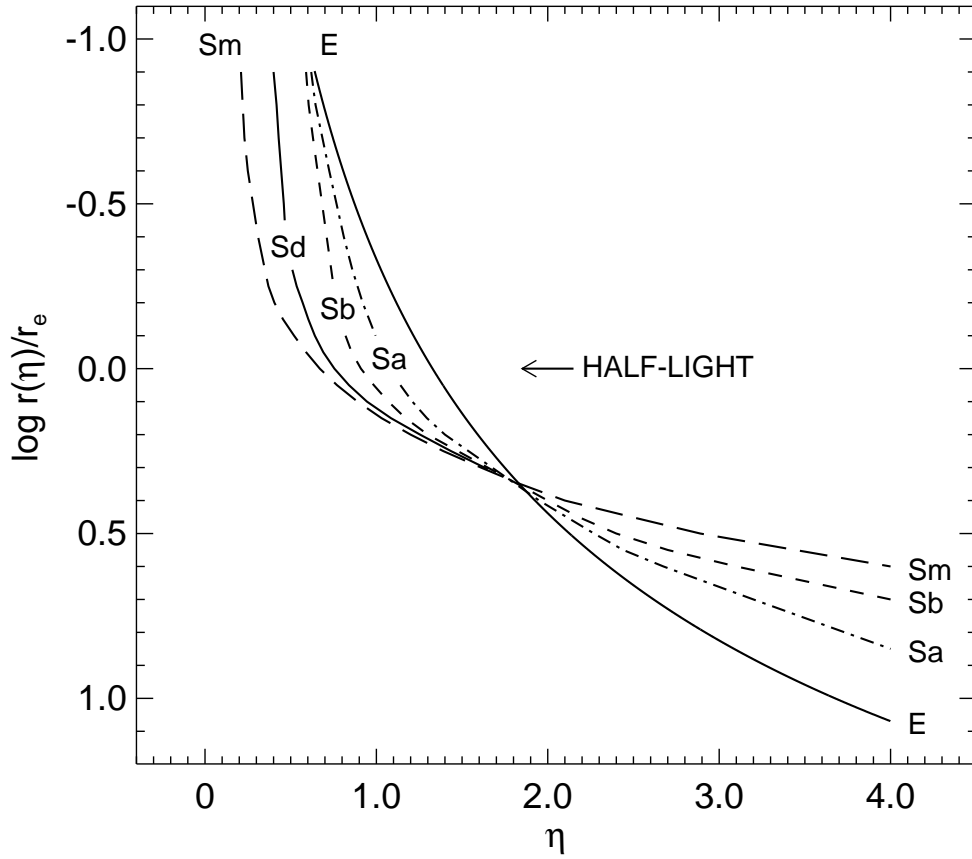


Fig. 1.— The variation of Petrosian η radii with the log of the ratio of the radius to the half-light radius for different galaxy types. The data are from Table 1.

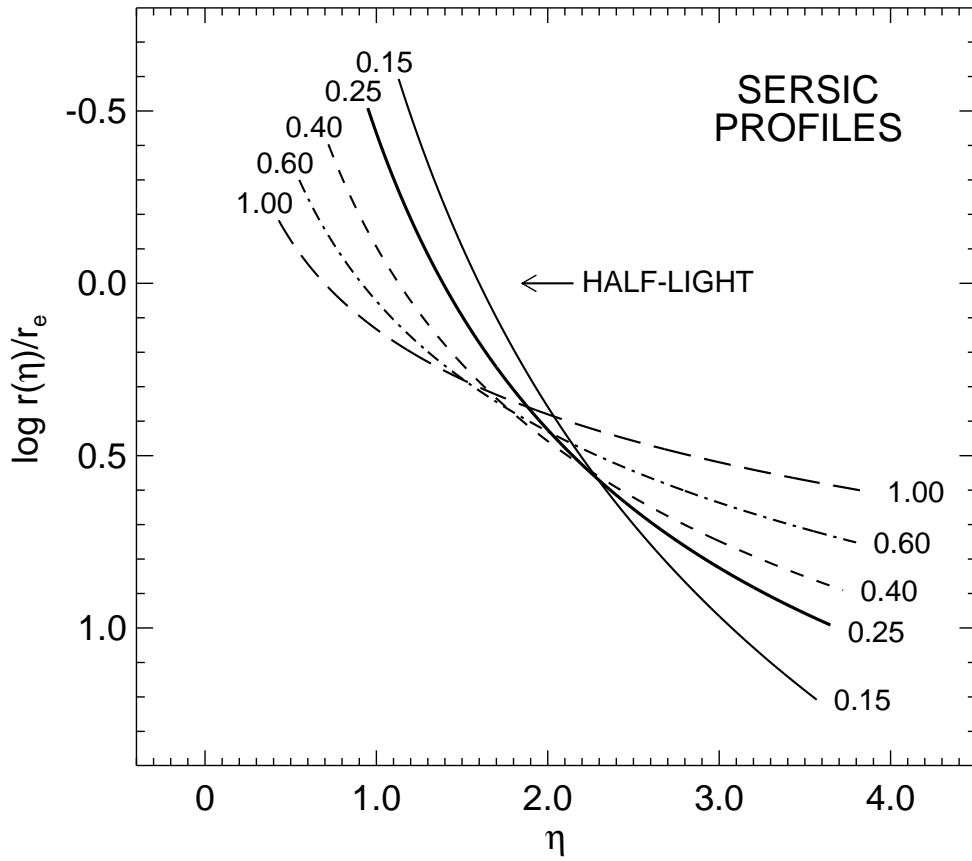


Fig. 2.— Relation between $\log r/r_e$ and η for the family of Sérsic profiles with different Sérsic exponents. Data are from Table 3. Note the similarity to Figure 1 for the different Hubble types.

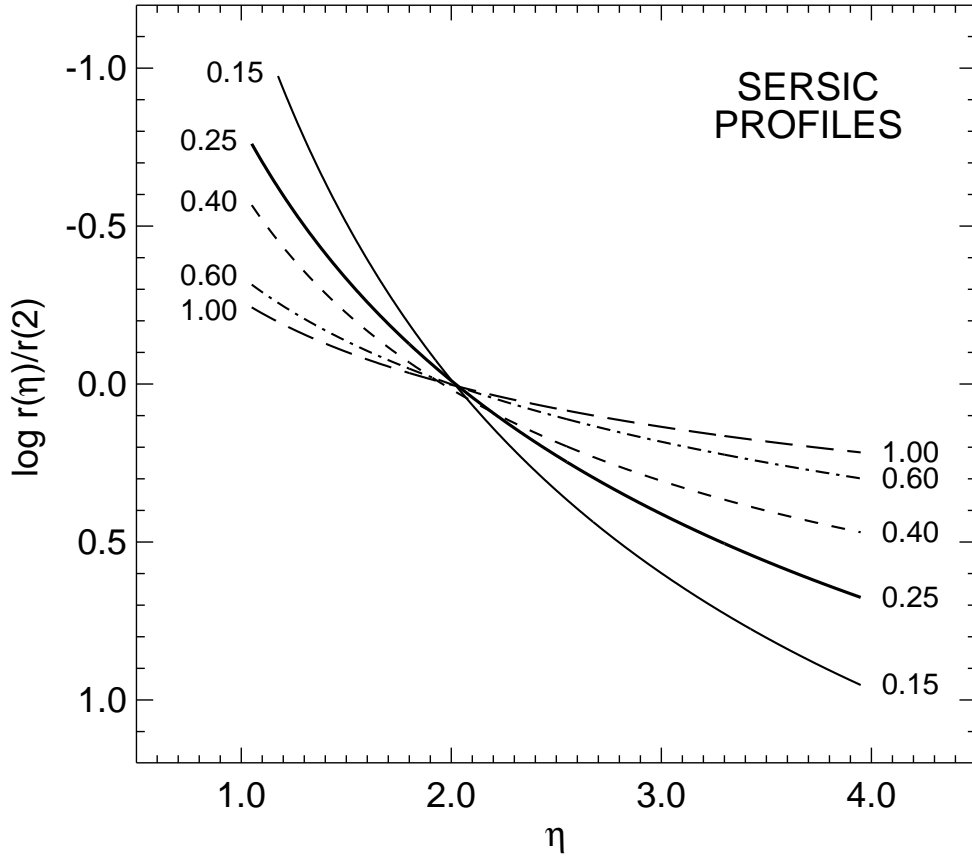


Fig. 3.— Correlation of η with the $\log r(\eta)/r(2)$ radii ratio for six Sérsic profiles from the data in Table 4.

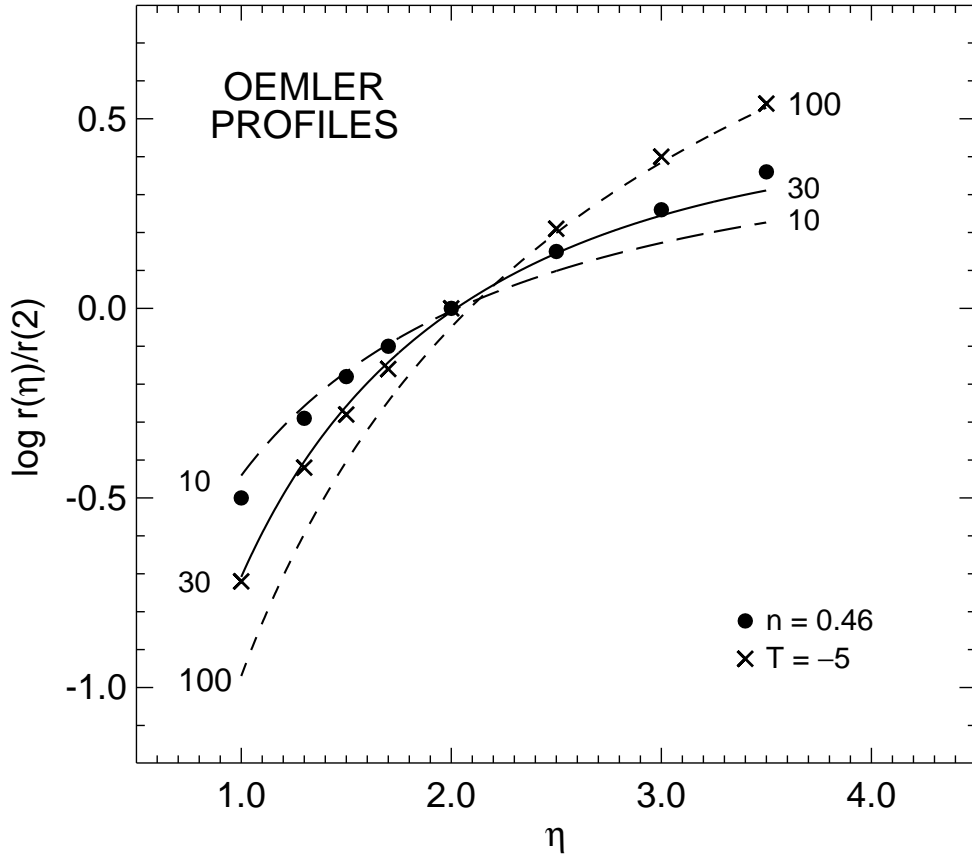


Fig. 4.— Three Oemler profiles in $\log r/r(2)$ vs. η compared with the observed $T = -5$ (giant E) galaxy profile and the $n = 0.46$ Sérsic profile. The data are from Tables 3 and 5.

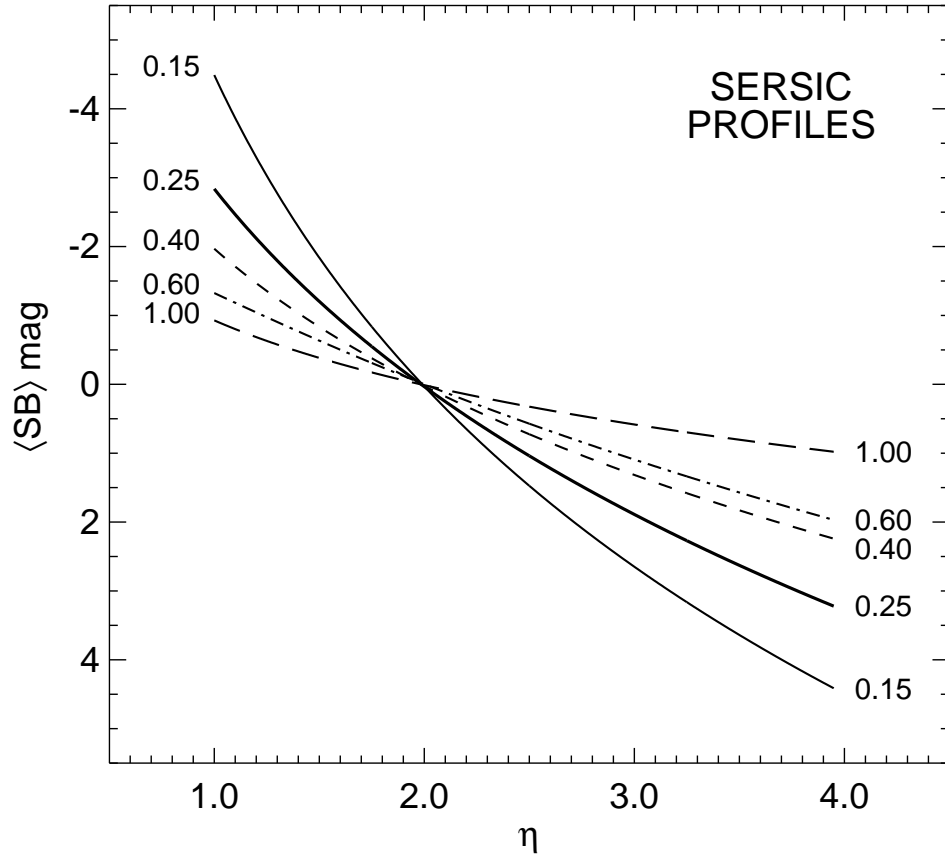


Fig. 5.— Correlation of $\langle SB \rangle$ with Sérsic n values from Table 6.

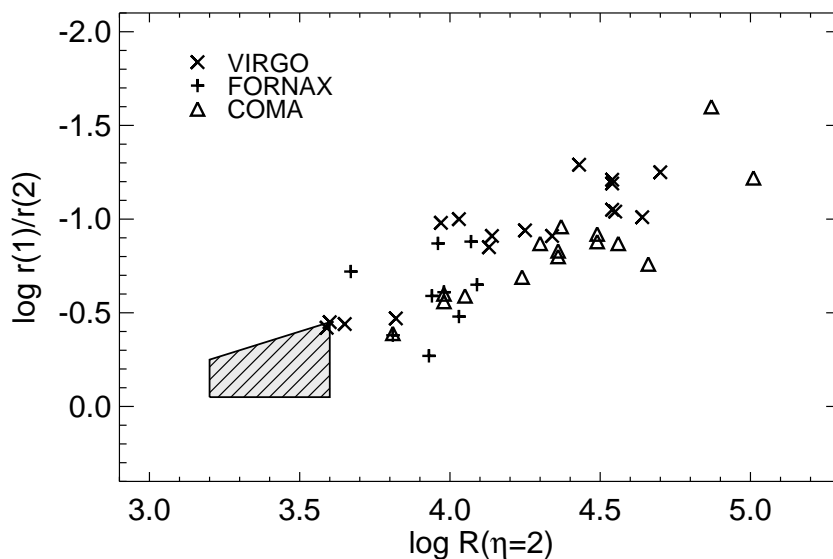


Fig. 6.— Variation of the $\log r(\eta = 1)/r(2)$ radius ratio with intrinsic diameter in pc for the Virgo (skipping jack crosses), Fornax (Roman crosses), and Coma cluster galaxies (triangles) from the data in Tables 1–3 of SP90b. The region of the dwarf dE galaxies for $\log R < 3.6$ is hatched. Interpolating in the diagnostic Table 4, or using Figure 3, shows that n for E and dE galaxies varies between 0.15 and 1.0 over the range of $\log R(2)$ between 3.3 and 4.8.

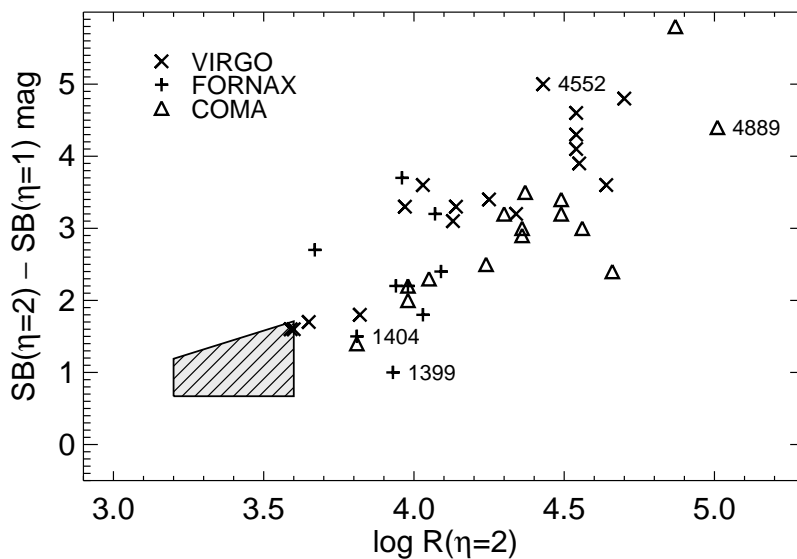


Fig. 7.— Same as Figure 6 but for the surface brightness differences between $\eta = 1$ and 2 for Virgo, Fornax, and Coma from the data in Tables 1–3 in SP90b.

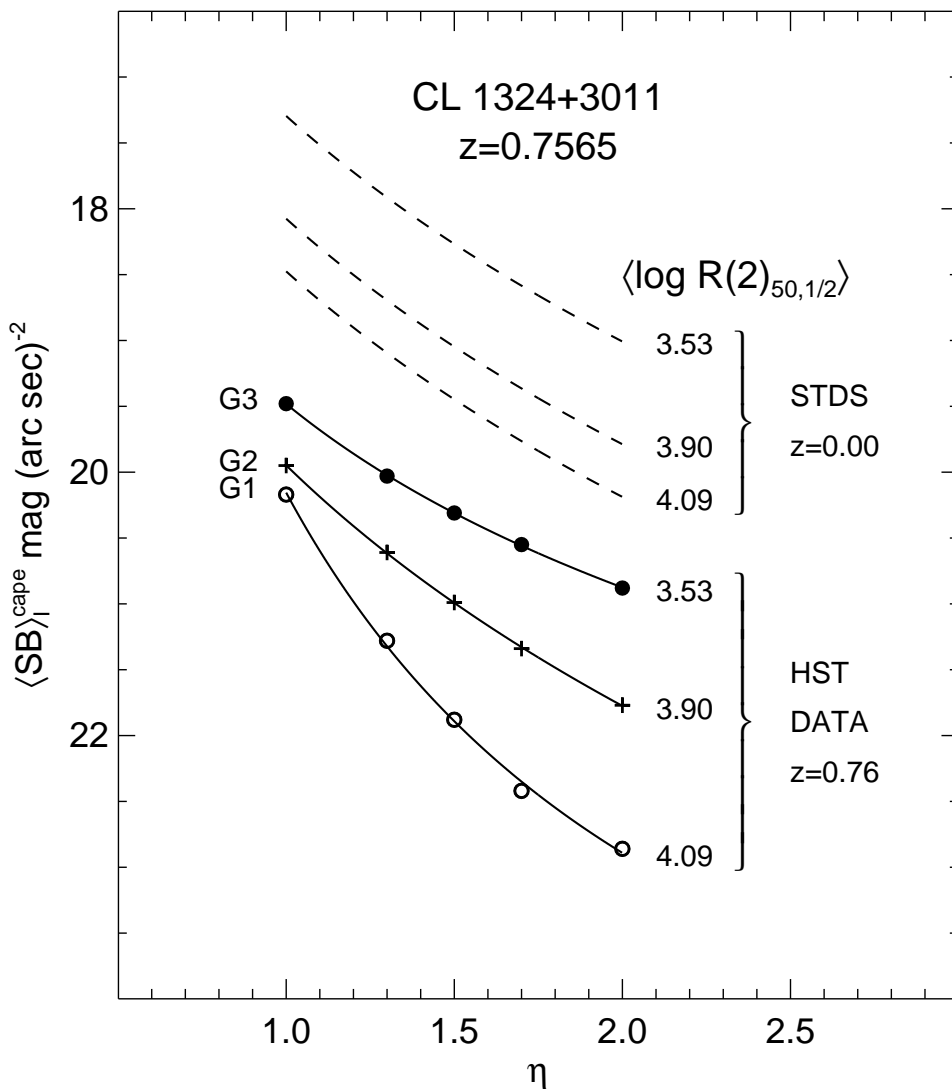


Fig. 8.— Surface brightness in the Cape/Cousins I band vs. η for galaxies in CL 1324+3011 ($z = 0.7565$) for three different intrinsic radii bins at $\eta = 2.0$. Standard zero-redshift curves at the listed radii, $R(2)$, for an $n = 0.46$ Sérsic profile are the dashed curves near the top, listed in Table 10. Smooth curves with the same shape are put through the observed data (Table 9) in the lower part of the diagram. Data are from Tables 9 and 10.

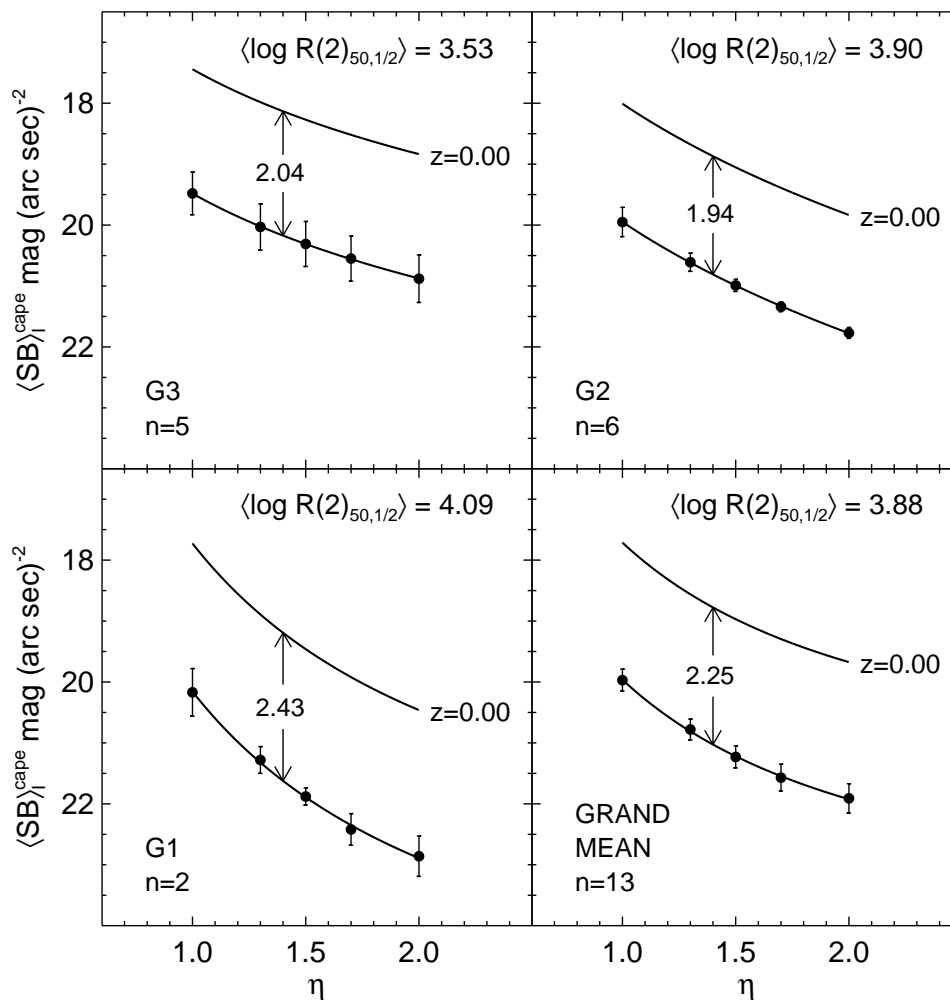


Fig. 9.— The data from Figure 8 plotted separately for the three radius bins and for the mean for Cl 1324+3011. The shape of the standard profile at each mean radius is dropped onto the data from the upper curves, zero pointed at $\eta = 1.5$.

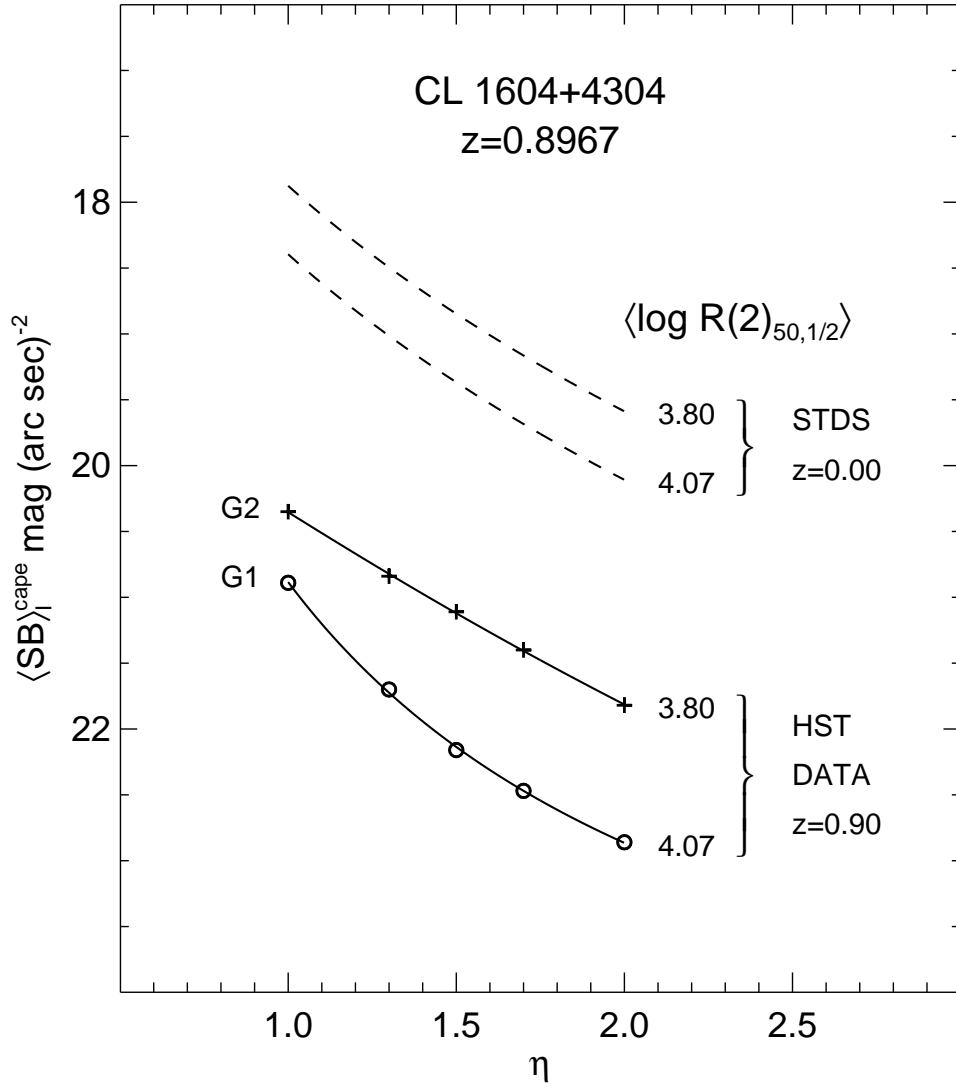


Fig. 10.— Same as Figure 8 but for Cl 1604+4304. Data are from Tables 11 & 12.

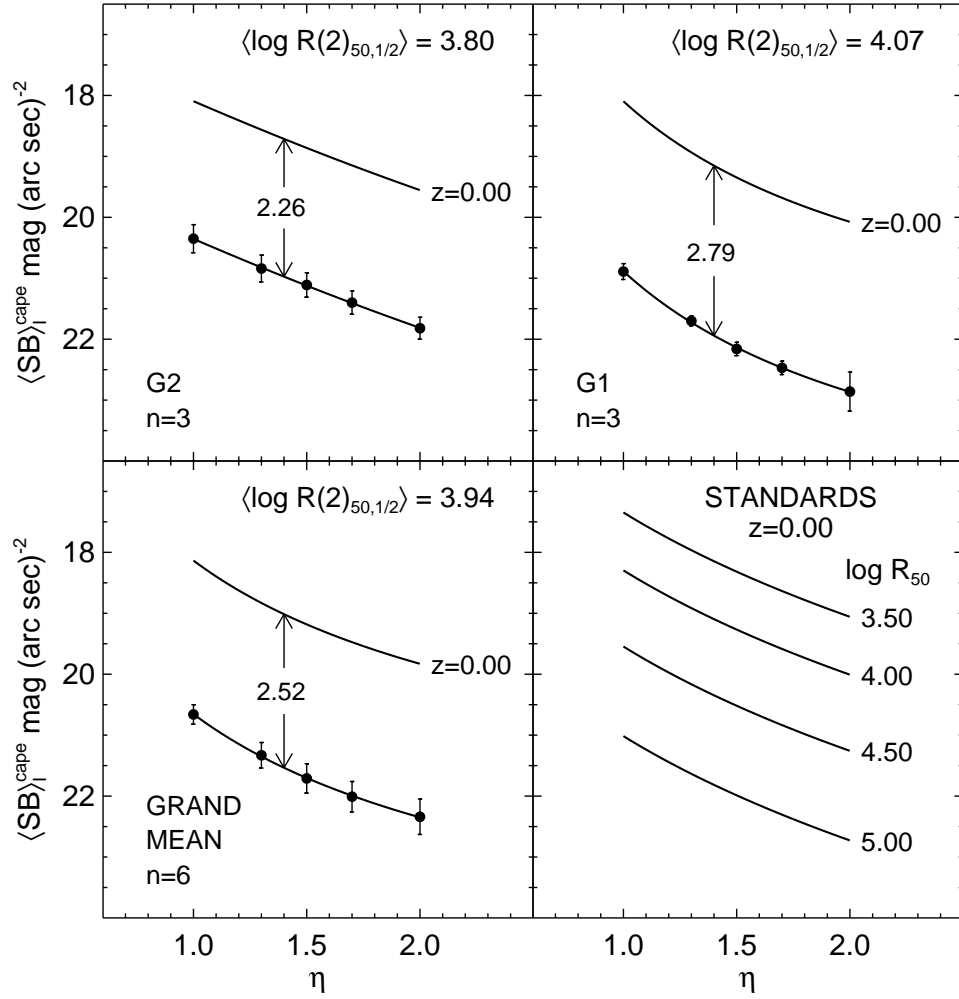


Fig. 11.— Same as Figure 9 but for Cl 1604+4304. Data are from Tables 11 & 12.

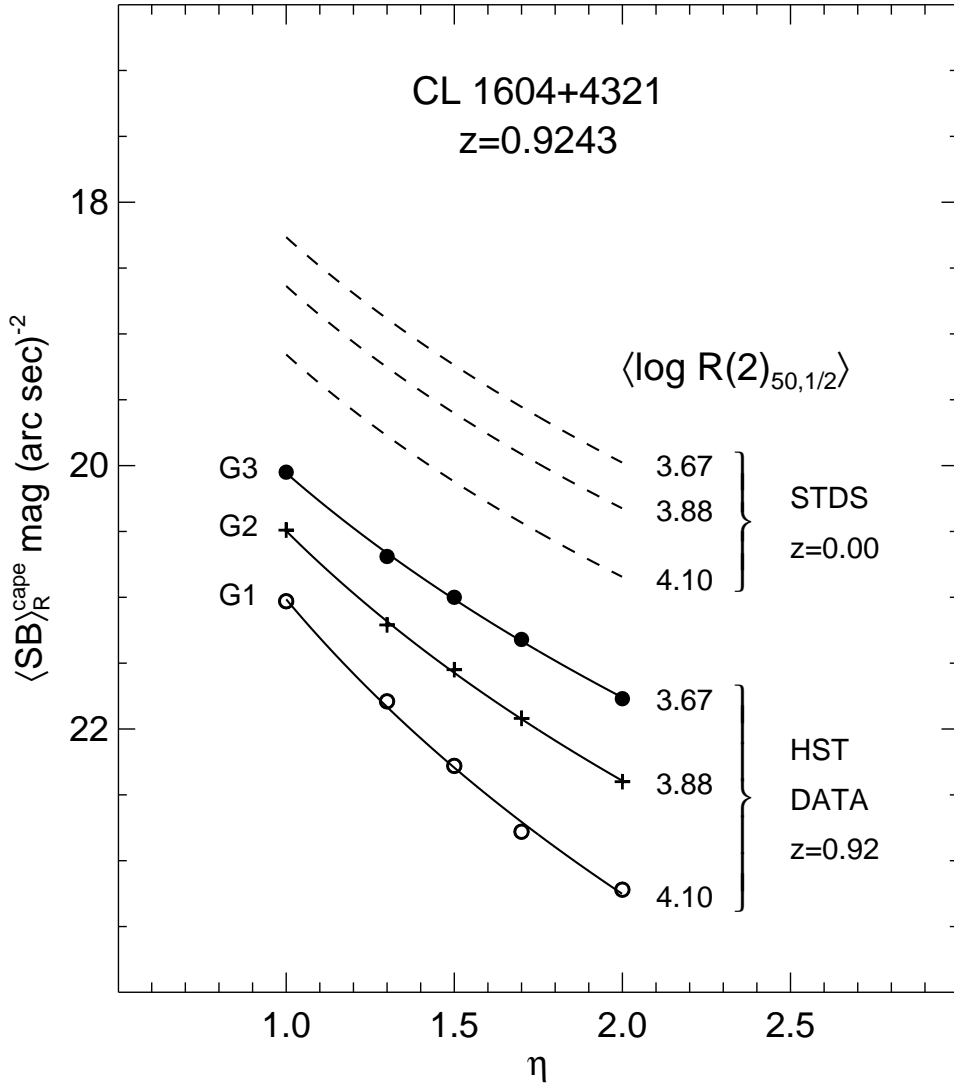


Fig. 12.— Same as Figure 8 but for Cl 1604+4321. Data are from Tables 13 & 14.

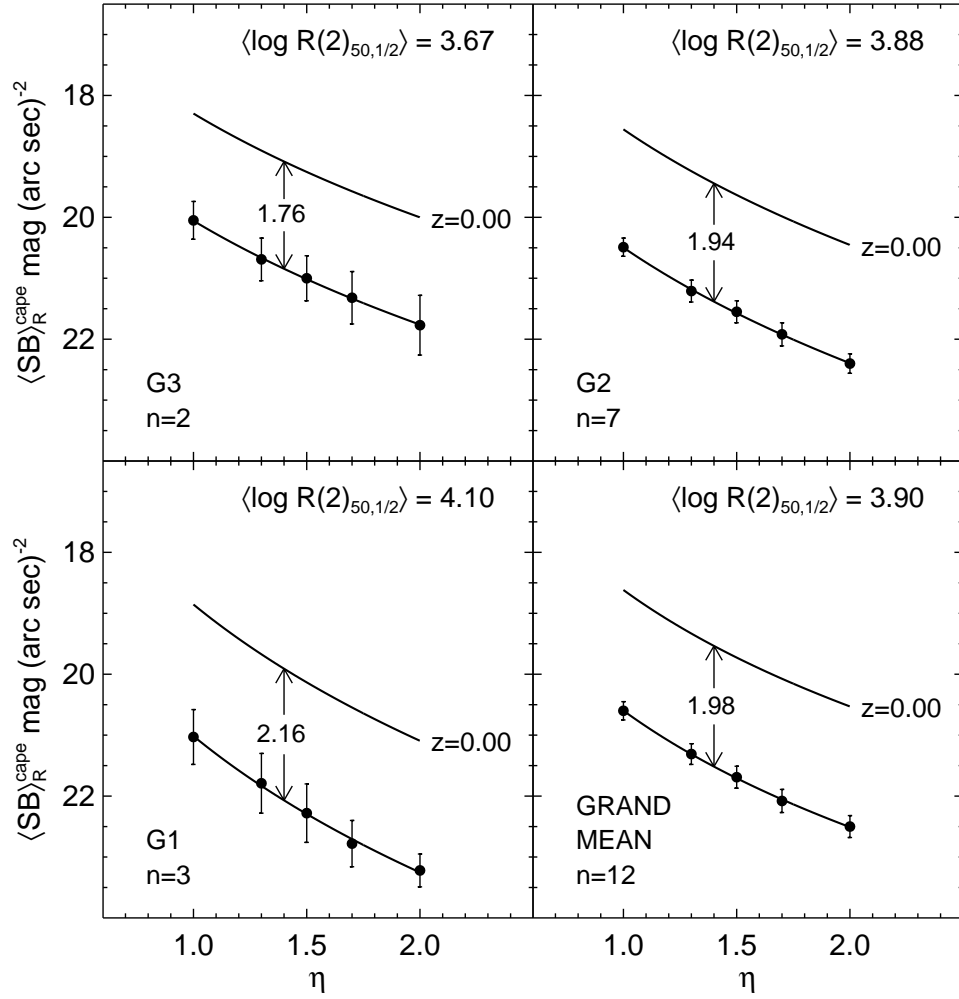


Fig. 13.— Same as Figure 9 but for Cl 1604+4321. Data are from Tables 13 & 14.

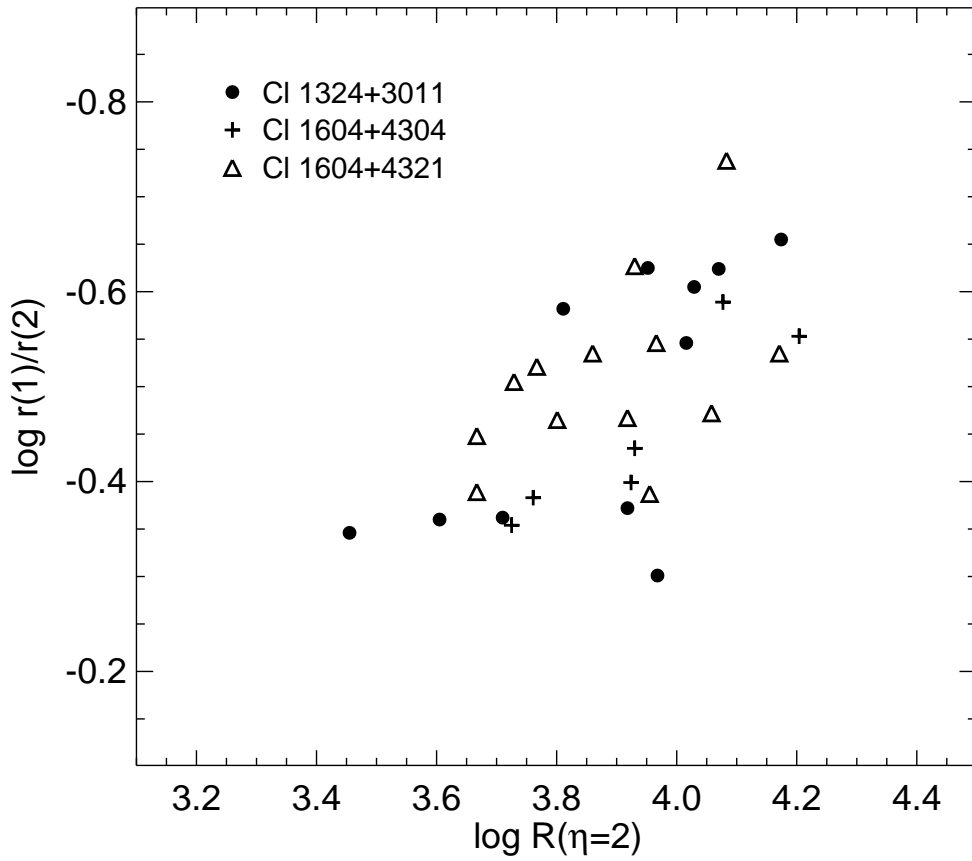


Fig. 14.— Variation of $\log R(1)/R(2)$ with $\log R(2)$ for galaxies in the three remote *HST* clusters. Dots are for Cl 1324+3011, roman crosses are for Cl 1604+4304, open triangles are for Cl 1604+4321. Data are calculated from Tables 2–4 of LS01c.

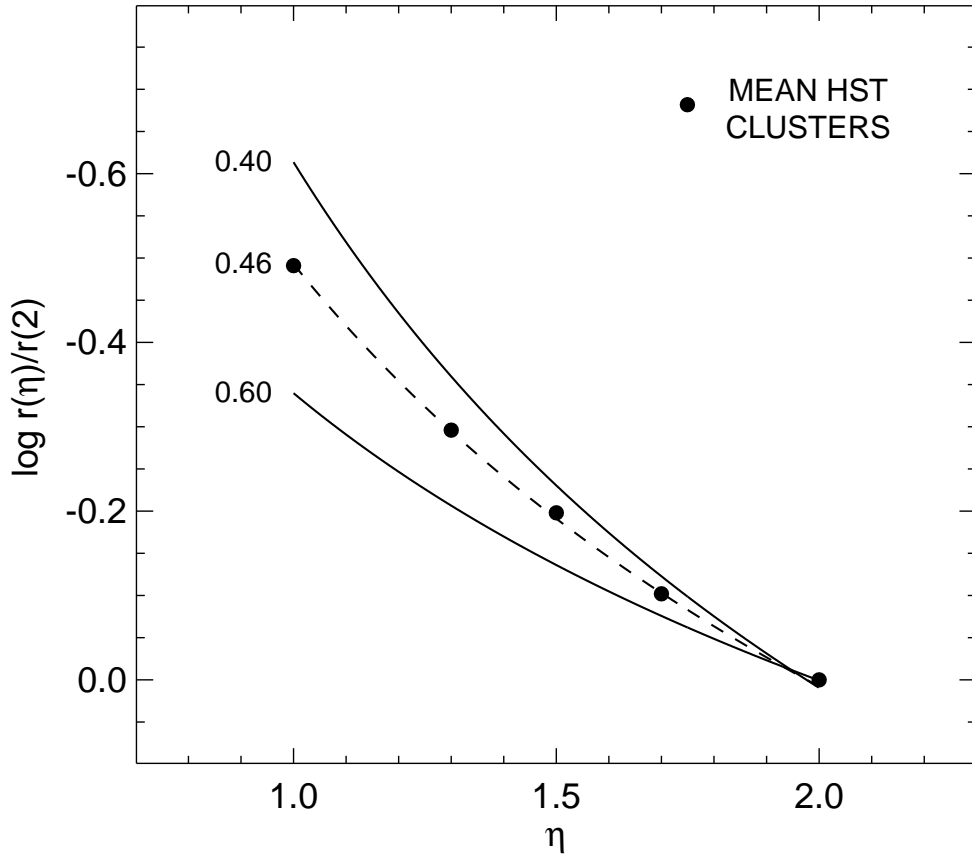


Fig. 15.— The run of the observed η values with $\log r(\eta)/r(2)$ averaged over all intrinsic radii for the galaxies in the *HST* clusters. The Sérsic functions for n between 0.4 and 0.6, from Table 4, are shown for comparison. From this, we deduce that the mean Sérsic exponent, averaged all radii for the *HST* cluster galaxies, is $n = 0.46$.